Eur. Phys. J. C (2026) 86:186
https://doi.org/10.1140/epjc/s10052-026-15389-6

THE EUROPEAN PHYSICAL JOURNAL C

Regular Article - Theoretical Physics

Repulsive anisotropy and global monopoles as gatekeepers of traversable wormhole models with modified gravitational insights

M. Yousaf[1,2,a], **G. Mustafa**[3,4,b], **A. Ditta**[5,c], **Asalkhon Alimova**[6,7,d], **Farruh Atamurotov**[8,9,e]

[1] Department of Mathematics, Virtual University of Pakistan, 54-Lawrence Road, Lahore 54000, Pakistan
[2] Research Center of Astrophysics and Cosmology, Khazar University, 41 Mehseti Street, 1096 Baku, Azerbaijan
[3] Department of Physics, Zhejiang Normal University, Jinhua 321004, People's Republic of China
[4] Zhejiang Institute of Photoelectronics and Zhejiang Institute for Advanced Light Source, Zhejiang Normal University, Jinhua 321004, Zhejiang, People's Republic of China
[5] Department of Mathematics, School of Science, University of Management and Technology, Lahore 54000, Pakistan
[6] National Research University TIIAME, Kori Niyoziy 39, 100000 Tashkent, Uzbekistan
[7] University of Tashkent for Applied Sciences, Str. Gavhar 1, 100149 Tashkent, Uzbekistan
[8] Kimyo International University in Tashkent, Shota Rustaveli Str. 156, 100121 Tashkent, Uzbekistan
[9] Urgench State University, Kh. Alimdjan Str. 14, 220100 Urgench, Uzbekistan

Received: 15 September 2025 / Accepted: 31 January 2026

Abstract The influence of three distinct shape functions on the physical properties of anisotropic wormholes (WHs) with a global monopole charge (GMC) is investigated in the background of minimally coupled modified gravity. The essential geometric criteria for traversability are assessed by confirming the throat condition and the flareout requirement. The GMC parameter's effect on the WH throat and surrounding curvature is visualized through 2D and 3D embedding diagrams which reveal that larger monopole values yield wider throats and smoother spatial curvature. To examine the feasibility of such WH models, we solve the modified field equations and analyze the classical energy conditions with relativistic corrections. Our analysis shows that the anisotropy parameter remains positive in all three cases, indicating a repulsive geometry, while this anisotropic repulsion counteracts gravitational collapse and supports the throat's stability. Additionally, the volume integral quantifier estimates the total exotic matter (EM), demonstrating that only negligible amounts are necessary to maintain traversable geometries due to modified gravitational insights.

1 Introduction

A decade after the introduction of special relativity [1], Einstein advanced his ideas in 1915 through the formulation of the general theory of relativity (GR) [2]. GR provides reinterpretation of gravity and enhance our ideas regarding the expanding universe, the dynamics of black holes, gravitational waves, and the formation of large-scale cosmic structures [3–6]. Compelling evidence from independent cosmological observations [7–10] revealed that the universe is undergoing accelerated expansion. These observations challenge the predictions of GR in its conventional form. To resolve this discrepancy, cosmologists introduced the concept of dark energy (DE), which is hypothesized to drive the observed acceleration by counteracting gravitational attraction on cosmic scales [11–15]. As a key element of the ΛCDM model, DE reshaped our understanding of the universe's evolution and ultimate fate; however, its true nature, whether as a cosmological constant, a dynamical field such as quintessence, or a manifestation of modified gravity theories (MGTs), remains an open question in modern physics.

To overcome the shortcomings of GR in explaining cosmic acceleration and other large-scale phenomena, numerous MGT frameworks developed which include investigations of dense source distribution limits in GR [16], curvature quintessence via DE some type of exponential potentials [17], unified DE models via cosmography [18], the broader class of MGTs [19], another MGT like $F(R)$ gravity with Lorentz-violating cosmological histories [20], com-

[a] e-mails: myousaf.math@gmail.com; m.yousaf@vu.edu.pk
[b] e-mail: gmustafa3828@gmail.com (corresponding author)
[c] e-mail: mradshahid01@gmail.com
[d] e-mail: asalxon2197@gmail.com
[e] e-mail: atamurotov@yahoo.com

Published online: 26 February 2026

prehensive reviews of MGT and cosmology [21], mimetic R-gravity addressing inflation, DE, along with bounces of universe [22], concise overviews of inflation to late time cosmic evolution [23], and a set of new smooth junction conditions in $f(G,T)$ gravity [24]. Furthermore, recent developments span diverse topics, including transparent boundary conditions for stationary Schrödinger equations in the background of Weyl–Titchmarsh MGT [25], particle acceleration in a specific type of black hole, i.e., Bocharova–Bronnikov–Melnikov–Bekenstein, studied in [26]. While wave-packet dynamics in monolayer graphene were investigated in [27], Zahid et al. [28] studied the shadow along with quasinormal mode constraints on rotating-type black holes by using some observations of M87* as well as Sgr A*. Additionally, they studied bulk viscous matter in $f(T)$ the MGT model as a route to acceleration of our universe [29]. Asad et al. [30] discussed the evolution of nonstatic fluid for irreversible gravitational radiation in Palatini $F(R)$ gravity and stellar dynamics with modified gravity theory, while the impact of $f(R)$ functions on the dynamical evolution of self-gravitating stars in [31], implications of anisotropic fluid composition along with MGTs, and electric charge alongside modeling compact objects studied in [32–36].

The GR faces difficulties in fully accounting for the observed accelerated expansion without invoking unknown components like DE; consequently, interest has grown in developing MGT models that extend or revise the GR framework, in which one prominent approach replaces the Ricci scalar R in the Einstein–Hilbert action with a general function $f(R)$ [37–39], while another avenue, $f(G)$ gravity, generalizes GR by incorporating the Gauss–Bonnet invariant G [40,41]. Additionally, $f(\tau)$ gravity, a branch of teleparallel gravity, describes gravitational interactions through torsion rather than curvature, replacing the torsion scalar τ with a function $f(\tau)$ [42,43]. Further models explore explicit couplings between space-time geometry and matter or scalar fields, departing from the standard GR paradigm where geometry and matter interact solely through the Einstein field equations, and some other MGTs [44–46] provide a good understanding of the universe's expanding behavior. The $f(R,T)$ theory proposed by Harko et al. [47] by incorporating the Ricci scalar R, and the trace of the energy–momentum tensor (EMT) T and its field equations are derived using the widely adopted metric formalism accounting for the coupling between matter and geometry. A specific formulation of the type $f(R,T) = f_1(R) + f_2(T)$ discussed in [48], while Chakraborty [49] revisited $f(R,T)$ gravity by incorporating stress energy conservation under both general and specific energy conditions, whereas Zaregonbadi [50] explored a minimal matter geometry coupling model to account for dark matter (DM) effects at galactic scales. Also, this framework effectively describes the formation of compact stars at both theoretical and astrophysical levels investigated in [51,52]. Sahoo et al. [53] studied the Bianchi type-I cosmological model within $f(R,T)$ gravity. Furthermore, this work expanded the application of $f(R,T)$ gravity to a variety of astrophysical and compact objects, including static spheres and cylinders like WHs, strange stars, and charged cylinder-type gravastars, as well as the thermodynamic properties of black holes, WHs, and neutron stars [54–60].

The WHs are hypothetical space-time tunnels envisioned as pathways linking distant regions of the universe, and these are some particular solutions of Einstein's field equations within GR. They hypothetically offer shortcuts that circumvent the usual constraints of cosmic distances. This extraordinary possibility arises because WHs, in theory, manipulate the geometry of space-time itself. Effectively, it creates a bridge between widely separated points, depending on their specific configuration. Furthermore, WHs may link remote galaxies, different epochs in time, or even parallel universes. The study of this type of compact objects extending the boundaries of known physics. In 1916, Ludwig Flamm [61] analyzed the Schwarzschild solution to Einstein's field equations and identified not only the theoretical basis for black holes but also proposed the existence of white holes and a connecting passage, later termed a WH. In 1935, Einstein and Rosen [62] developed this concept further. They introduced the Einstein–Rosen bridge, which described a non-traversable connection between two regions. Later, in 1973, Ellis [63] and Bronnikov [64] independently found solutions involving a massless scalar field, resulting in the well-known Ellis drainhole, whereas a major advancement occurred with the work of Morris and Thorne [65], who outlined traversable WHs supported by EM capable of sustaining an open throat, theoretically enabling transit between spatially separated regions or parallel universes. Hochberg and Visser [66,67] subsequently investigated dynamic WHs, identifying the presence of two throats and confirming that violation of the null energy constraints is universal and essential for traversability, extending this analysis to rotating WHs studied in [68]. In the Brans–Dicke framework [69,70], WHs exhibit both static and dynamic behavior, the latter driven by evolving scalar fields, whereas thin-shell WHs, along with electromagnetic fields and modified Chaplygin gas with relativistic corrections examined in [71,72] and Yousaf et al. [73] studied GMC induced WHs in power-law gravity, their stability, and physical viability.

Theoretical studies on WHs expanded beyond GR, with the aim of minimizing or eliminating the requirement for EM. Thus improving the prospects for physically realizable traversable WHs, and the condition $R = 0$ (with R as the four-dimensional Ricci scalar) generates a variety of static, spherically symmetric Lorentzian WH solutions with different throat sizes and symmetries demonstrated in [74]. Such traversable and globally regular WHs were examined within braneworld scenarios, satisfying vacuum Einstein equations

on the brane while incorporating effective stress–energy contributions from bulk gravitational effects. Lemos et al. [75] explored WHs with a non-zero cosmological constant, analyzing boundary matching, WH mass, and surface pressure for predetermined traversal conditions by employing specific shape functions. The thin-shell WHs in the context of heterotic string theory using the Darmois–Israel formalism, computing surface stresses, and assessing linearized stability studied in [76]. The traversable WH solutions with nonstatic conformal and spherical symmetries, using defined shape functions and equations of state to localize EM near the throat, suggest that only minimal energy condition violations are required investigated in [77]. While imprints of GMC in Morris–Thorne type WHs and energy conditions under the influence of higher-dimensional gravity are studied in [78]. Almatroud and his collaborators [79] studied electromagnetic fields and fuzzy WH models, along side decoupling of anisotropic WHs via MGD in the presence of DM haloes in [80], while WHs construction through the diverse DM density profiles investigated in [81].

Within the framework of $f(\tau)$ gravity, where τ denotes torsion, Daouda et al. [82] analyzed the equations of motion for anisotropic space-time, deriving new spherically symmetric solutions for both black holes and WHs under constant torsion conditions. While novel insights into WH solutions in extended teleparallel gravity inspired by non-commutative geometry studied in [83]. Saleem and his collaborators [84] investigated new relativistic traversable WHs and energy constraints in the Rastall Teleparallel gravitational paradigm. Although Harko et al. [85] established general conditions within MGT models that allow WH solutions without the necessity of EM, showing that higher-order curvature effects can act as an effective gravitational fluid that supports the WH geometry. Bambi et al. [86], working in $f(R)$ gravity with Born–Infeld electrodynamics under the Palatini formalism, demonstrated that central singularities in spherically symmetric configurations may be replaced by finite-size WHs, resulting in geodesically complete spacetimes with implications for the cosmic censorship conjecture, while an exponential $f(R,T)$ model yields WH solutions consistent with energy conditions introduced in [87]. While Sahoo et al. [88] proposed a hybrid shape function for WHs in $f(R,T)$ gravity, analyzing both anisotropic and isotropic scenarios along with equilibrium-based stability, Chawla et al. [89] examined traversable WH geometries supported by a logarithmic shape function within exponential $f(R,T)$ gravity, exploring three-parameter regimes and energy condition characteristics through comprehensive dynamical and graphical analysis. Recently, Tangphati et al. [90] investigated WH metrics in $f(R,T)$ gravity by comparing alternative matter Lagrangians, producing asymptotically well-behaved WH solutions. Furthermore, quantum, Euclidean, ring, non-orientable, artificial WHs, and the existence of traversable WHs in the minimally coupled gravity model, along with other MGTs remain active topics of theoretical inquiry across multiple disciplines [91–97].

In this study, we investigate the theoretical construction of traversable WH solutions with minimally coupled $f(R,T)$ gravity model which incorporates three distinct contributions. The first one is ordinary matter. The second one may be considered as curvature modifications via the $f(R)$ dependence. The third one is additional matter geometry coupling through the T dependence. Firstly, we establish the theoretical groundwork by deriving the full set of modified field equations in $f(R,T)$ gravity. It also includes the formulation of throat conditions and flaring-out criteria. Secondly, we develop a solution methodology by specifying suitable forms of the matter Lagrangian and the $f(R,T)$ function, followed by the derivation of exact WH solutions, while thirdly, we perform a thorough physical analysis by evaluating the effective stress EMT, systematically studying energy condition behaviors. We characterize the resulting space-time geometries through both analytical and graphical techniques. And finally, our analysis using the Volume Integral Quantifier (VIQ) provides a quantitative assessment of the EM content required to sustain the considered traversable WH geometries. However, the results reveal that for all three shape function models, the EM is predominantly concentrated in the vicinity of the WH throat, with the VIQ magnitude decreasing as the radial coordinate increases. Furthermore, the dependence of the parameter on the correction term ϖ and the GMC parameter ζ highlights that smaller values of these parameters consistently reduce the general content of EM, thus improving the physical viability of stable and traversable WHs in the background of the chosen gravitational framework $f(R,T)$ gravity.

2 Theoretical framework of $f(R,T)$ gravity: field equations and energy conditions

2.1 Formalism of $f(R,T)$ theory and Morris–Thorne type WH

The $f(R,T)$ MGT extends GR by allowing the gravitational Lagrangian to depend not only on the Ricci scalar R but also on the trace of the EMT T which additional dependence introduces new dynamical features into the gravitational sector. Several analyses showed that $f(R,T)$ models can suppress the growth of cosmic structures in a way consistent with local observations, while more recent investigations indicate that this class of MGTs may provide a compelling alternative to the standard cosmological model by potentially alleviating tensions between cosmic microwave background data and measurements of large-scale structure, yielding growth rates that differ from those predicted by ΛCDM. While adopting

the general form of the $f(R,T)$ action as formulated in [47], we write:

$$\mathcal{I}_{f(R,T)} = \frac{1}{2}\int_{\Omega} \frac{f(R,T)}{8\pi G}\sqrt{-g}d^4x + \mathcal{I}^{(m)}. \tag{1}$$

In this framework, Ω denotes a four-dimensional space-time manifold that, while locally resembling flat Euclidean space, can possess global curvature, whereas the coordinates x^{ξ}, where the variation of the Greek letter ξ can be taken as $(\xi = 0, 1, 2, 3)$ are defined on Ω, with x^0 representing the temporal component and x^1, x^2, x^3 corresponding to spatial dimensions. Within this MGT, the usual Ricci scalar R is generalized through a functional dependence on both R and the trace T of the EMT, introducing higher-order or nonlinear corrections that directly couple matter to geometry.

The determinant g of the metric tensor $g_{\xi\varpi}$ defines the invariant space-time volume element, while G the gravitational constant characterizes the strength of gravitational interactions, while the matter action in this theory is written as $\mathcal{I}^{(m)} = \int \mathcal{L}_{(m)}\sqrt{-g}\, d^4x$, where the matter Lagrangian density $\mathcal{L}_{(m)}$ represents the matter Lagrangian density, governing the dynamics and interactions of matter fields, whereas the factor $\sqrt{-g}\, d^4x$ ensures coordinate invariance of the action. In our considered MGT, this matter action is not only coupled to the geometry via the metric $g_{\xi\varpi}$ but also interacts explicitly with T, thereby inducing a direct interdependence between matter content and space-time curvature, and this interaction remains consistent with the Einstein equivalence principle while introducing new dynamical degrees of freedom. This modification enriches the gravitational dynamics, providing a mechanism to describe the accelerated expansion of the universe without invoking a cosmological constant, whereas with suitable choices of $f(R,T)$, one can reproduce effects usually attributed to DE and even obtain a natural framework for early cosmic inflation, all within a theory that incorporates explicit matter geometry coupling via T. By varying the modified action (Eq. (1)) with respect to the metric tensor, we derive the corresponding field equations in the form:

$$G_{\xi\varpi} = \frac{1}{f_R}\Big[(f_T+1)T^{(m)}_{\xi\varpi} - g_{\xi\varpi}\mu f_T + \frac{1}{2}(f - Rf_R)g_{\xi\varpi} + (\nabla_{\xi}\nabla_{\varpi} - g_{\xi\varpi}\Box)f_R\Big], \tag{2}$$

where $f_R \equiv \partial f/\partial R$ and $f_T \equiv \partial f/\partial T$. Also, $G_{\xi\varpi}$, ∇_{ξ} and $T^{(m)}_{\xi\varpi}$ are the usual Einstein tensor, covariant derivative, and usual matter, respectively, while our considered case study $T^{(m)}_{\xi\varpi}$ describing an anisotropic fluid structure is formulated as

$$T^{(m)}_{\xi\varpi} = (p_t+\mu)\mathcal{U}_{\xi}\mathcal{U}_{\varpi} + p_t g_{\xi\varpi} + (p_r - p_t)\Upsilon_{\xi}\Upsilon_{\varpi}, \tag{3}$$

here, μ is energy density, p_r and p_t represents pressures in respective directions, while $\mathcal{U}^{\xi}$ and Υ^{ξ} are the velocity four-vector and radial vector, respectively, with the following constraints:

$$\mathcal{U}^{\xi} = (1,0,0,0),\ \ \mathcal{U}^{\xi}\mathcal{U}_{\xi} = -1,\ \ \text{and}\ \ \Upsilon^{\xi}\Upsilon_{\xi} = 1,\ \ \text{also,}$$
$$\mathcal{U}^{\xi}\Upsilon_{\xi} = 0,\ \Upsilon^1 = \xi\sqrt{1-\frac{A(r)}{r}},\ \ \Upsilon^0 = 0 = \Upsilon^2 = \Upsilon^3. \tag{4}$$

In both GR and MGTs, the line element serves as a key mathematical construct that characterizes the geometry of space-time. It defines how to calculate the infinitesimal distance between two points within a chosen coordinate system. A spherically symmetric line element in Schwarzschild coordinates (t, r, θ, ϕ) [65] is described by

$$ds^2 = \sum_{\xi,\varpi\approx t,r,\theta,\phi} g_{\xi\varpi}dx^{\xi}dx^{\varpi} = -e^{2\Phi(r)}dt^2 + \frac{dr^2}{\zeta^2\left(1-\frac{A(r)}{r}\right)} + r^2\sum_{i,j\approx\theta,\phi}\hat{g}_{ij}dx^i dx^j,$$
$$\sum_{i,j\approx\theta,\phi}\hat{g}_{ij}dx^i dx^j = d\theta^2 + \sin^2\theta d\phi^2, \tag{5}$$

the metric tensor under consideration, which serves as an analytical framework for investigating Lorentzian WH geometries. The first term of (5) is known as the time component, which contains the redshift function $\Phi(r)$, and governs gravitational time dilation throughout space-time. Radial variations $\Phi(r)$ produce $\Phi(r)$ position-dependent clock rates, with the extreme case $e^{2\Phi(r)} \to 0$ at some radius $r = r_h$ indicating event horizon formation. For traversable WH solutions, we enforce the constraint $\Phi(r) =$ constant (equivalently $\Phi'(r) = 0$), which both prevents horizon formation and ensures the absence of singularities along the throat. This condition guarantees that proper time measurements remain finite and continuous for all observers traversing the WH. The second term of (5) as a radial component determines how distances change in the radial direction; here, $A(r)$ indicates the shape function, which determines the spatial geometry of the WH throat and controls the structure of the space-time geometry and ζ is the GMC parameter arising due to the breaking of symmetry [98]. Inverse trigonometric shape functions and less-complex WH configurations in D-dimensional Einstein gravity were studied in [99], and imprints of GMC on the stability and energy conditions of traversable WH models in $f(R)$ gravity were discussed in [100], while Asad and collaborators [101] investigated traversable WHs in $f(R)$ gravity and the influence of GMC on the energy conditions. The third and fourth terms of (5) are angular components and describe the spatial structure in the angular directions

and standard spherical symmetry, these components remain unchanged from the Schwarzschild metric, whereas the presence of these terms ensures that the WH is spherically symmetric. There must be no event horizon for a traversable WH, so we consider the case with a constant redshift function, i.e., $\Phi'(r) = 0$. We can put $\Phi(r) = 0$ without any loss of generality. Thus, the line element reduces to:

$$\begin{aligned} ds^2 &= \sum_{\xi,\varpi\approx t,r,\theta,\phi} g_{\xi\varpi} dx^{\xi} dx^{\varpi} = -dt^2 + \frac{dr^2}{\zeta^2\left(1-\frac{A(r)}{r}\right)} \\ &\quad + r^2 \sum_{i,j\approx\theta,\phi} \hat{g}_{ij} dx^i dx^j, \\ &\quad \sum_{i,j\approx\theta,\phi} \hat{g}_{ij} dx^i dx^j = d\theta^2 + \sin^2\theta d\phi^2, \end{aligned} \tag{6}$$

The time component of the metric, which is now flat, indicating the absence of gravitational time dilation and allowing both observers and signals to traverse the WH unimpeded. Rewriting the above line element in the compact form $ds^2 = g_{\xi\varpi}\, dx^{\xi} dx^{\varpi}$, the metric tensor and its inverse can be expressed as

$$\begin{aligned} g_{\xi\varpi} &= \mathrm{diag}\left(-1,\ \frac{r}{\zeta^2(r-A(r))},\ r^2,\ r^2\sin^2\theta\right), \\ g^{\xi\varpi} &= \mathrm{diag}\left(-1,\ \zeta^2\left(\frac{r-A(r)}{r}\right),\ \frac{1}{r^2},\ \frac{1}{r^2\sin^2\theta}\right). \end{aligned} \tag{7}$$

2.2 Modified Einstein equations

All required mathematical framework described above, now varying indices in Eq. (2) and utilizing the Einstein tensor $G_{\xi\varpi}$, the Ricci scalar $R = g^{\xi\varpi} R_{\xi\varpi}$ calculated for our metric (6), the field equations in our modified $f(R,T)$ framework after rigorous calculation and simplification are:

$$\begin{aligned} \frac{-\zeta^2 + \zeta^2 A'(r) + 1}{r^2} &= \frac{1}{2r^2 f_R} \\ &\times \Big[-\zeta^2 r A'(r) f'_R - 3\zeta^2 A(r) f'_R - 2\zeta^2 r A(r) f''_R \\ &+ 2\zeta^2 r^2 f''_R + 4\zeta^2 r f'_R \\ &+ 2r^2\big(2f_T + 1\big)\mu + r^2 f_R R(r) - r^2 f \Big], \end{aligned} \tag{8}$$

$$\begin{aligned} \frac{\zeta^2 A(r) + \zeta^2(-r) + r}{\zeta^2 r^2 (A(r) - r)} &= \frac{1}{2\zeta^2 r(r - A(r)) f_R} \\ &\times \Big[4\zeta^2 A(r) f'_R + 2r^2 f_T p_r - 2r^2 f_T \mu \\ &- r^2 f_R R(r) + r^2 f - 4\zeta^2 r f'_R \\ &+ 2r^2 p_r \Big], \end{aligned} \tag{9}$$

$$\begin{aligned} \frac{\zeta^2\big(A(r) - rA'(r)\big)}{2r} &= \frac{1}{2f_R} \\ &\times \Big[\zeta^2 r A'(r) f'_R + \zeta^2 A(r) f'_R + 2\zeta^2 r A(r) f''_R \\ &+ 2r^2 f_T p_t - 2\zeta^2 r^2 f''_R - 2r^2 f_T \mu \\ &- r^2 f_R R(r) - 2\zeta^2 r f_R + r^2 f + 2r^2 p_t \Big], \end{aligned} \tag{10}$$

$$\begin{aligned} \frac{\zeta^2 sin^2\theta\big(A(r) - rA'(r)\big)}{2r} &= \frac{sin^2\theta}{2f_R} \\ &\times \Big[\zeta^2 r A'(r) f'_R + \zeta^2 A(r) f'_R + 2\zeta^2 r A(r) f''_R + 2r^2 f_T p_t \\ &- 2\zeta^2 r^2 f''_R - 2r^2 f_T \mu \\ &- r^2 f_R R(r) - 2\zeta^2 r f_R + r^2 f + 2r^2 p_t \Big]. \end{aligned} \tag{11}$$

There are many $f(R,T)$ models explained by Harko [47] as, some of them are separable models $f(R)+f(T)$, multiplicative models, $f(R)f(T)$ and non-linear couplings $f(R,T) = R + \alpha R^m + \xi T^n$. Here, we have considered the function $f(R,T)$ of the form of the additive/separable model as

$$f(R,T) = R + 2\varpi T, \tag{12}$$

where ϖ represents correction parameter and the term $2\varpi T$ represents a linear coupling between matter and geometry. Solving the field equations (8), (9), and (10) along with the substitution of the $f(R,T)$ model and further simplification takes the form:

$$\mu(r) = -\frac{(2\varpi - 1)\big(-\zeta^2 + \zeta^2 A'(r) + 1\big)}{(4\varpi + 1)r^2}, \tag{13}$$

$$p_r(r) = -\frac{\begin{array}{c}-4\zeta^2\varpi(\varpi+1)rA'(r) + \zeta^2(4\varpi+1)A(r) \\ +\big(\zeta^2 - 1\big)\big(4\varpi^2 - 1\big)r\end{array}}{\big(8\varpi^2 + 6\varpi + 1\big)r^3}, \tag{14}$$

$$p_t(r) = \frac{\begin{array}{c}\zeta^2\big(8\varpi^2 + 4\varpi - 1\big)rA'(r) + \zeta^2(4\varpi+1)A(r) \\ -8\big(\zeta^2 - 1\big)\varpi(\varpi+1)r\end{array}}{2\big(8\varpi^2 + 6\varpi + 1\big)r^3}. \tag{15}$$

The Eqs. (13)–(15) are the expressions for energy density, radial and tangential pressure, respectively. Using these physical quantities and evaluating different energy conditions and anisotropy parameters with graphs, we will discuss the WH structures.

2.3 Condition of asymptotic flatness and so-called flare-out conditions

A shape function plays a central role in determining the geometry and physical characteristics of a WH. A fundamental requirement for constructing traversable WHs is the fulfillment of the flare-out condition at the throat. At sufficiently large radial distances from the WH throat, the spacetime should approach a flat geometry. This condition enables

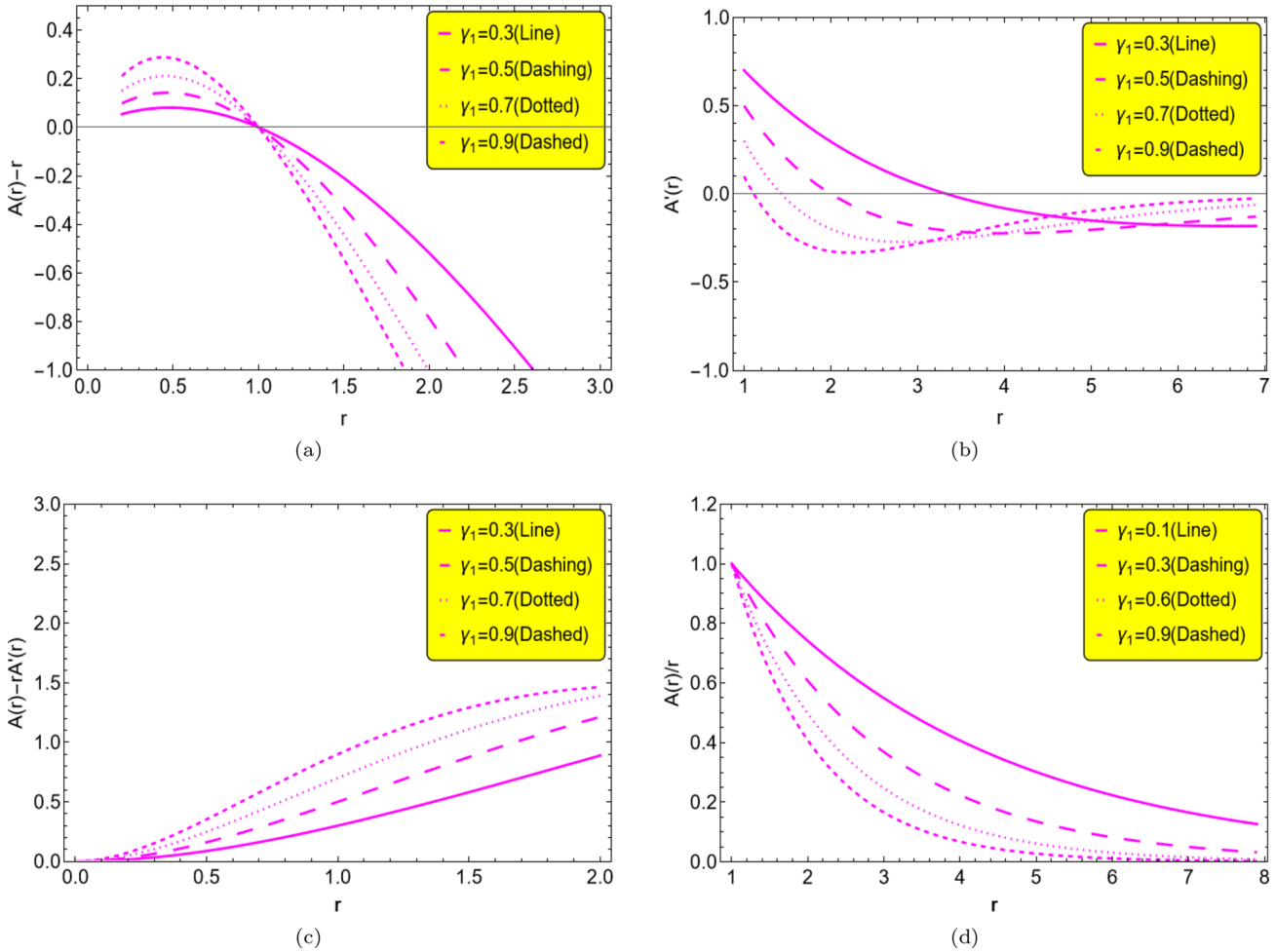

Fig. 1 Graphical representation of the flare-out condition of model 1 with varying values of ζ, i.e., $0 < \zeta < 1$, throat radius $a_0 = 1$

a smooth transition between the WH region and the asymptotically flat regions of the universe where gravitational effects become negligible. While a consistent and physically viable WH structure must satisfy the following criteria for the shape function $A(r)$:

- $A(r)/r < 1$ for all $r > a_0$, ensuring that the embedded surface flares outward,
- $A(r) = a_0$ at the throat radius $r = a_0$,
- $\lim_{r\to\infty} A(r)/r = 0$, ensuring asymptotic flatness,
- $A(r) - A'(r)\, r > 0$, a geometric requirement related to the embedded surface profile,
- $A'(r) < 1$ at $r = a_0$, guaranteeing that the flare-out condition holds at the throat.

In our analysis, we consider three distinct classes of shape functions, each of which is constructed to satisfy the flare-out and asymptotic flatness criteria. In this work, we considered and investigated three toy models of WH shape functions, defined as

$$A_1(r) = r\, e^{\gamma_1(a_0-r)} \quad \text{(Exponential Shape Function)}, \tag{16}$$

$$A_2(r) = a_0\left[\gamma_2\left(1 - \tfrac{a_0}{r}\right) + 1\right] \quad \text{(Polynomial Shape Function)}, \tag{17}$$

$$A_3(r) = a_0\left(\frac{r}{a_0}\right)^{\gamma_3} \quad \text{(Power-Law Shape Function)}, \tag{18}$$

where γ_1, γ_2, and γ_3 are parameter values of the shape function model, and a_0 denotes the radius of the throat of the WH, where as these shape function models $A_1(r)$, $A_2(r)$ and $A_3(r)$ are widely used in the literature [102–104]. To examine their physical viability, we evaluate basic criteria and plot the functions $A(r)-r$ vs r, $A'(r)$ vs r, $A(r)-A'(r)\, r$ vs r and $A(r)/r$ vs r in Figs. 1, 2, and 3, while corresponding embedded diagrams are presented in Figs. 4 and 5. For each model, we explore the influence of the GMC parameter $0 < \zeta < 1$ on the WH geometry. The panel (a) in each figure confirm that the throat radius remains fixed at $a_0 = 1$ which confirm the minimal radial coordinate remains consistent across all con-

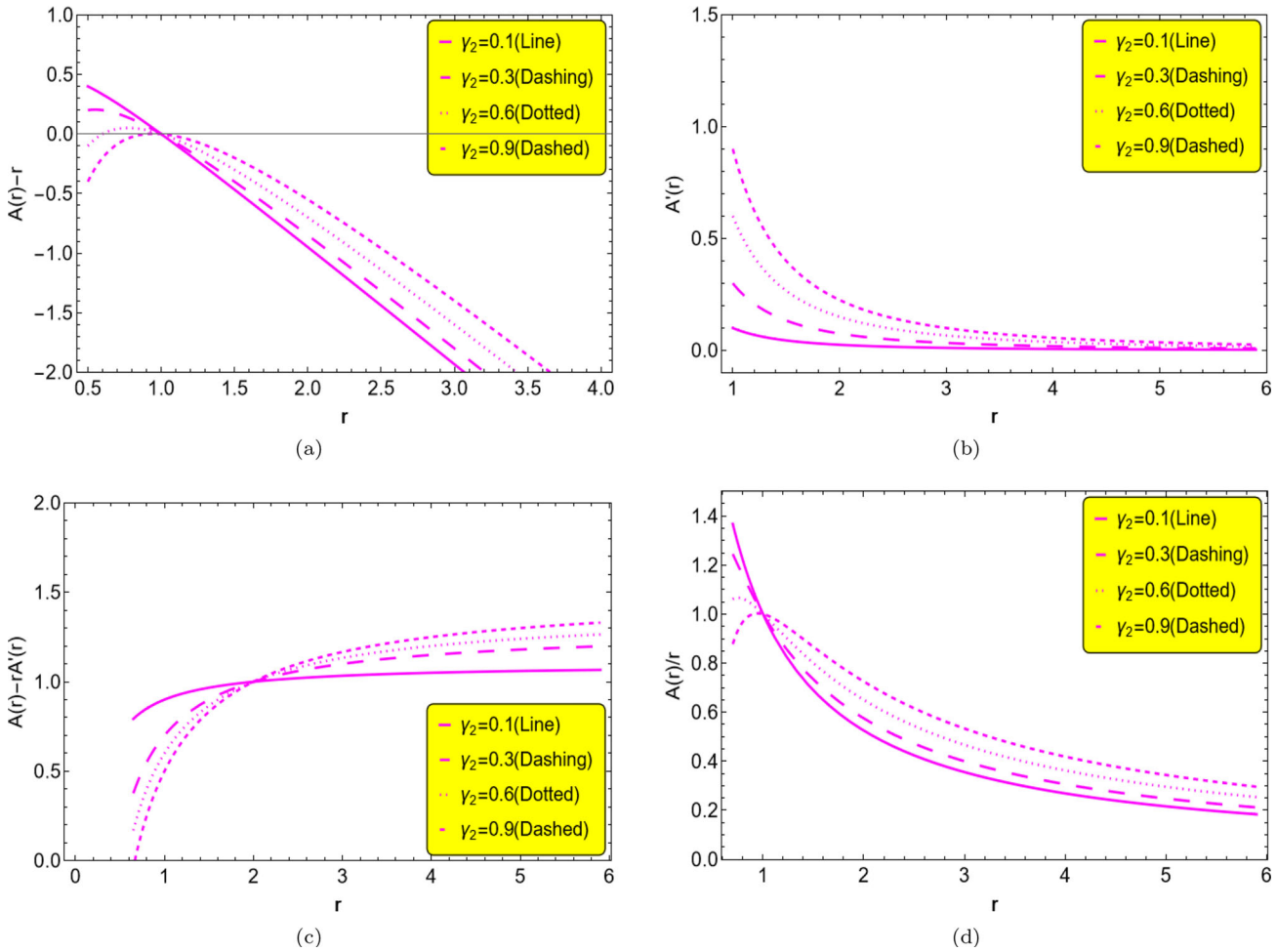

Fig. 2 Graphical representation of the flare-out of model 2 with varying values of ζ, i.e., $0 < \zeta < 1$, throat radius $a_0 = 1$

figurations. From Fig. 1, it is evident that the first toy model satisfies all the conditions required for a traversable WH. The behaviors of the second and third toy models exhibit similar characteristics, as in Figs. 2 and 3. Both models show acceptable behavior for $0 < \gamma_2 < 1$ and $0 < \gamma_3 < 1$. For the third model $(A_3(r))$, the graphs in Fig. 3 demonstrate analogous qualitative features. One can observe that as γ_3 increases, the behavior of $A(r)/r$ and $A(r) - A'(r)\, r$ follows the same general trends observed for $A_2(r)$, confirming the consistency and parameter sensitivity of these shape function models.

2.4 Embedding diagrams of three WH shape function models

To visualize the WH structure inherent in these models, we provide both 2D and 3D embedding diagrams [102,103,105]. The 3D plots represent surfaces of revolution constructed by embedding an equatorial spatial slice (t = constant, $\vartheta = \pi/2$) into Euclidean space, and the relevant spatial section of the WH metric is

$$ds^2 = \frac{dr^2}{\zeta^2\left(1 - \frac{A(r)}{r}\right)} + r^2 d\varphi^2, \tag{19}$$

which, when compared with the flat Euclidean metric in cylindrical coordinates,

$$ds^2 = dz^2 + dr^2 + r^2 d\varphi^2, \tag{20}$$

allows the embedding surface to be parameterized as $z = z(r)$, in this case, the induced metric reads

$$ds^2 = \left[1 + \left(\frac{dz}{dr}\right)^2\right] dr^2 + r^2 d\varphi^2. \tag{21}$$

By equating the two metrics, we obtain the embedding differential equation

$$\frac{dz}{dr} = \pm \sqrt{\frac{1}{\zeta^2\left(1 - \frac{A(r)}{r}\right)} - 1}, \tag{22}$$

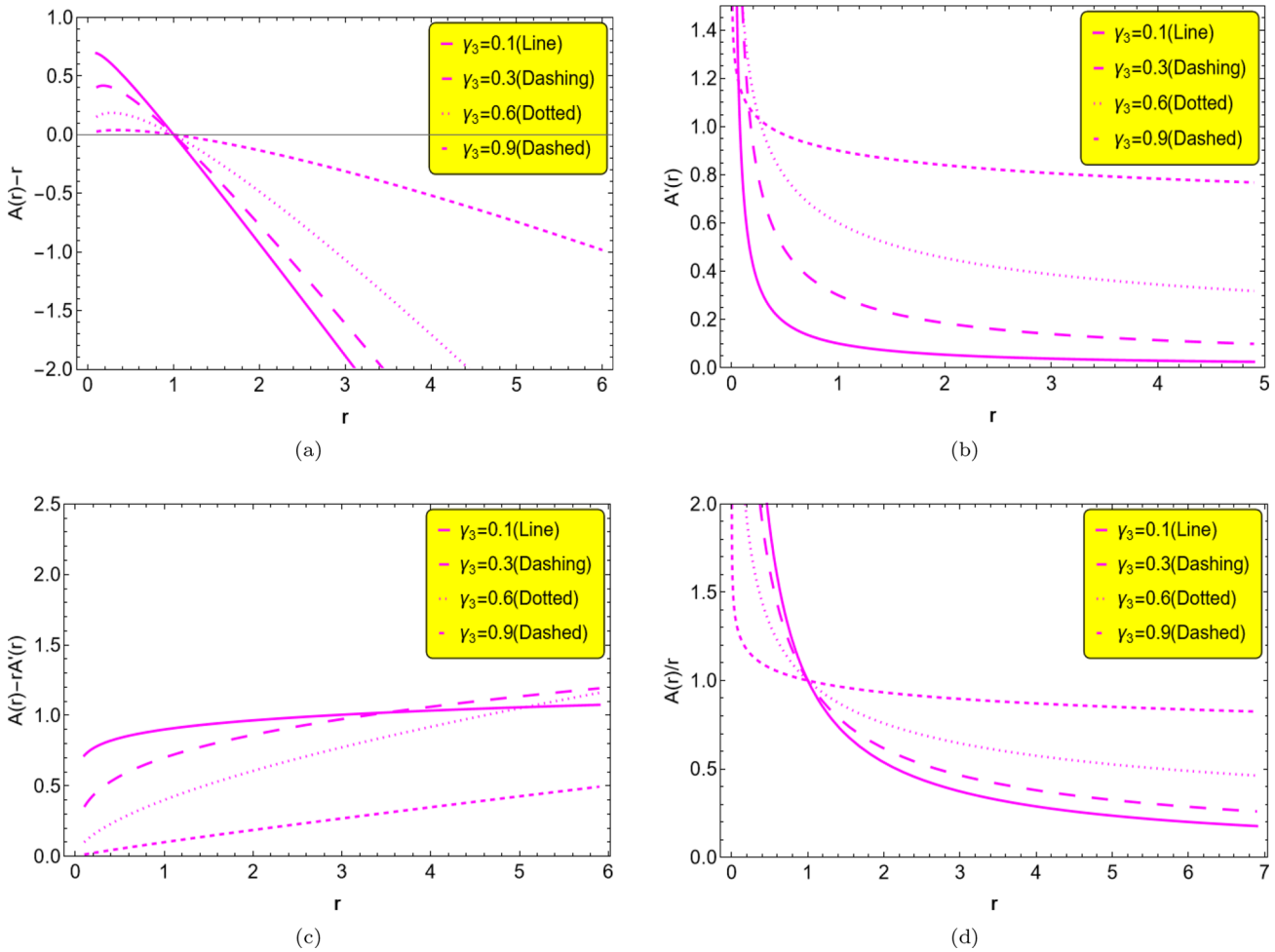

Fig. 3 Graphical representation of the flare-out condition of model 3 with varying values of ζ, i.e., $0 < \zeta < 1$, throat radius $a_0 = 1$

which governs the z profile of the embedded WH surface. The embedding diagrams corresponding to shape function models as given in Eqs. (16)–(18) are presented in Figs. 4 and 5 which highlight several essential geometric features. As one can observe that:

(a) In $(r = a_0)$, the embedded surface becomes vertical $(dz/dr \to \infty)$, which represents the flaring-out condition, as $r \to \infty$, the surface gradually flattens $(dz/dr \to 0)$, consistent with the asymptotic flatness.
(b) For suitable choices of shape functions parameters reveal their impact on the geometry of the WH. For Eq. (16), increasing γ_1 tends to reduce the vertical extent of the WH while modifying the curvature near the throat.
(c) Similarly, for Eq. (17), higher γ_2 values alter the surface profile. This variation affecting both the shape and the height of the WH. Also, for the third model, Eqs. (18), exhibits a comparable sensitivity. We can observe that by varying γ_3 reshapes the embedded surface and adjusts the flare and curvature of the WH throat.

Each embedding diagram depicts the upper and lower halves of the WH, representing two asymptotically flat regions that are smoothly connected at $r = a_0$.

3 Anisotropy in WH with relativistic corrections

In anisotropic matter distributions, the pressure anisotropy factor is defined as the difference between the tangential pressure and the radial pressure. An anisotropy parameter is denoted by $\Delta(r)$. There are three basic possibilities regarding its values, if $\Delta(r) = 0$, the matter distribution is isotropic, whereas $\Delta(r) \neq 0$ indicates anisotropy. Mathematically, the anisotropy parameter $\Delta(r)$ may be define in the following form:

$$\Delta(r) = p_t(r) - p_r(r). \tag{23}$$

In the case $\Delta(r) \neq 0$, there are two further cases that indicate the nature of anisotropy in different ways: The first one is considered as $\Delta(r) < 0$, it implying an attractive geome-

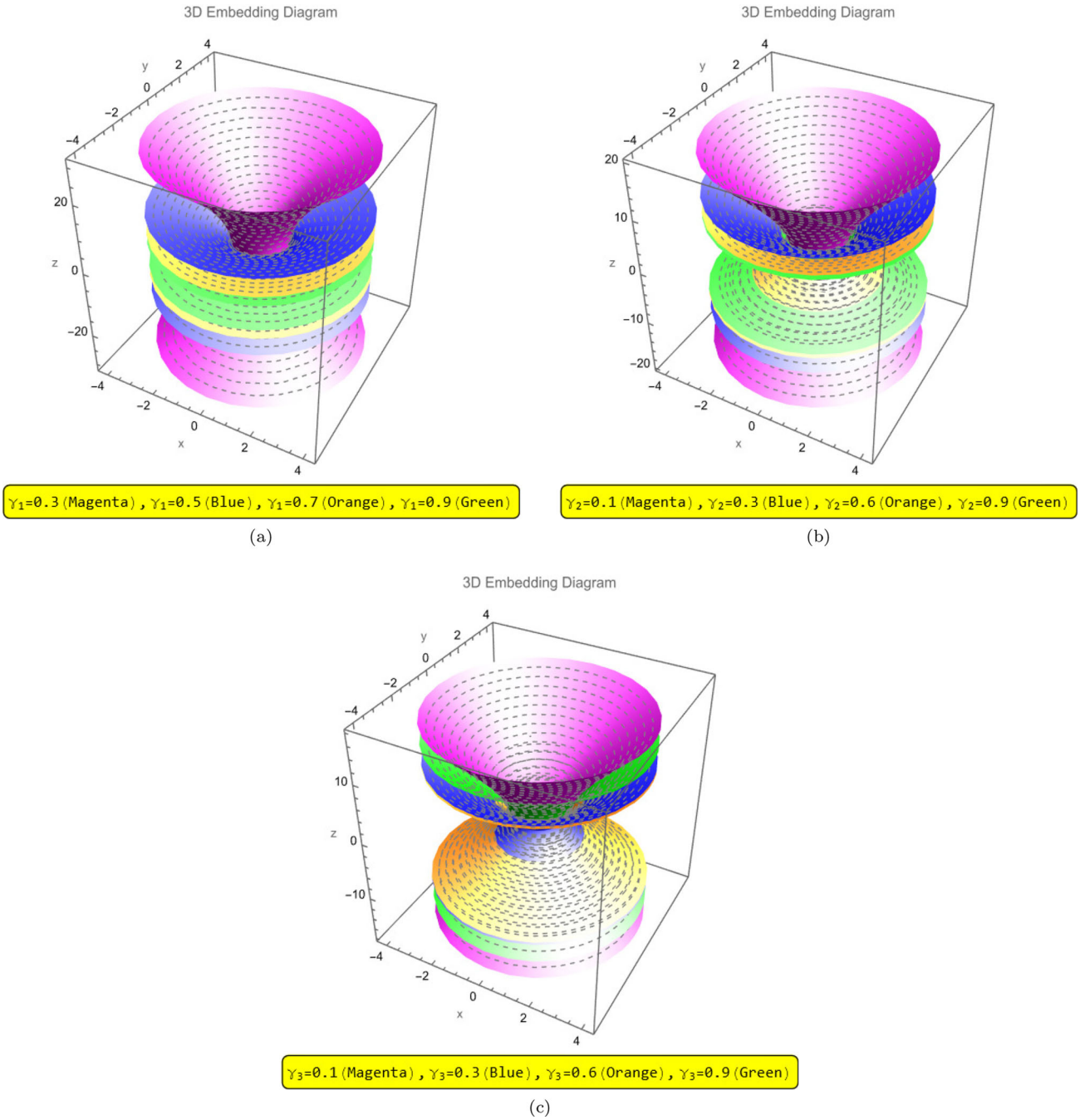

Fig. 4 3D profiles of embedding diagrams for $A_1(r)$ panel (**a**), $A_2(r)$ panel (**b**), and $A_3(r)$ panel (**c**) at $a_0 = 1$ with varying values of ζ, i.e., $0 < \zeta < 1$

try. While in second case it may consider $\Delta(r) > 0$, and it suggests a repulsive geometry. In the framework of $f(R, T)$ gravity, the effective field equations inherently modify the radial and tangential stresses due to the coupling between matter and geometry. These plots are essential in identifying whether anisotropy favors stability and supports the traversability of GMC WHs in the context of $f(R, T)$ gravity. The mathematical expression for the anisotropy parameter of our considered shape function Models$_{\{1,2,3,4,5,6\}}$ in the background of minimally coupled $f(R, T)$ gravitational model is calculated as follows:

$$\Delta_{\text{Model-1}}(r) = \frac{\zeta^2\left((\gamma_1 r + 2)e^{\gamma_1(a_0 - r)} - 2\right) + 2}{2(2\varpi + 1)r^2}, \tag{24}$$

$$\Delta_{\text{Model-2}}(r) = \frac{-2(\zeta^2 - 1)r^2 + 3(\gamma_2 + 1)\zeta^2 a_0 r - 4\gamma_2\zeta^2 a_0^2}{2(2\varpi + 1)r^4}, \tag{25}$$

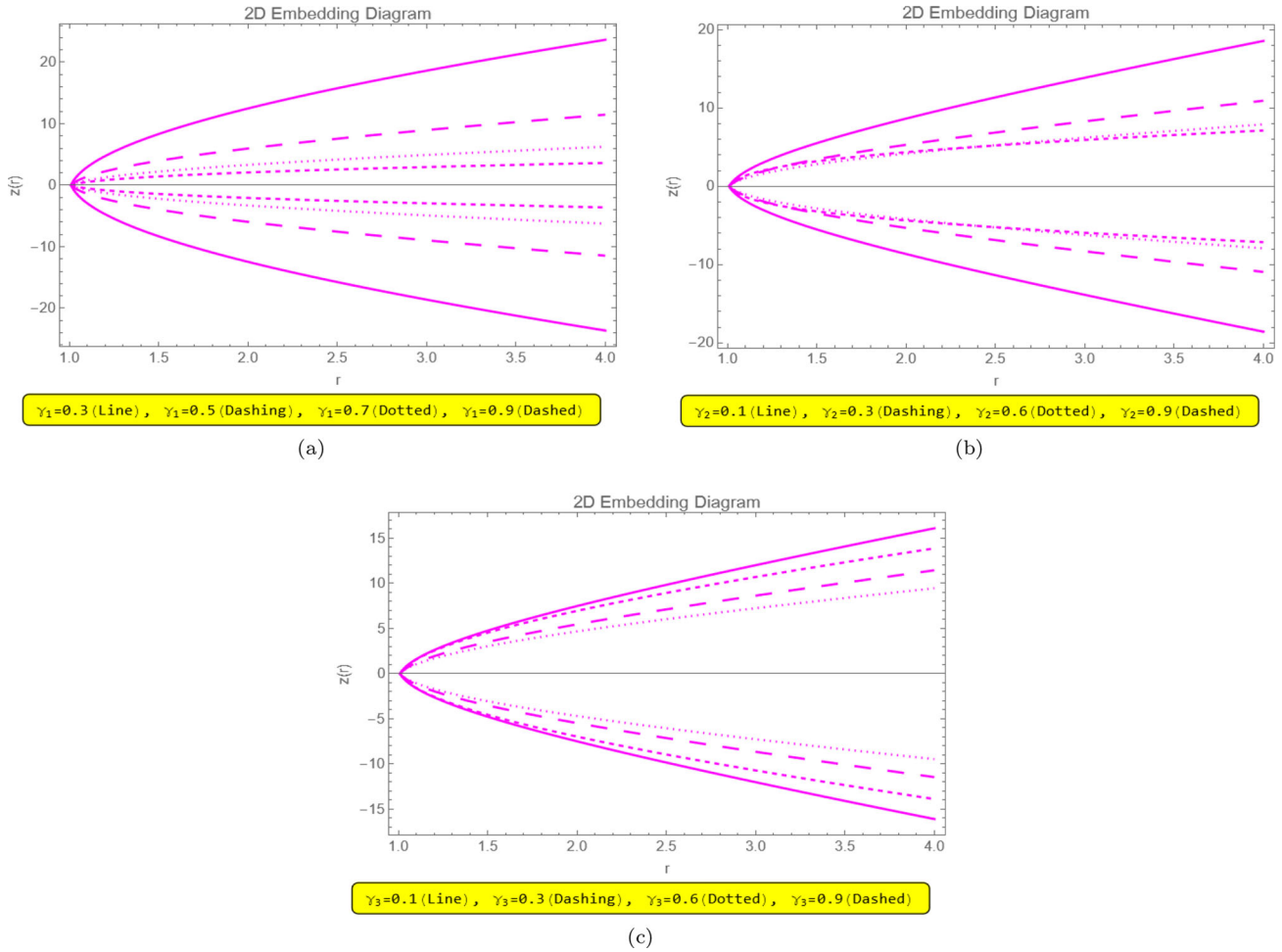

Fig. 5 Pictorial representation of 2D embedding diagrams of three shape function models $A_1(r)$ panel (**a**), $A_2(r)$ panel (**b**), and $A_3(r)$ panel (**c**) at $a_0 = 1$ with varying values of ζ, i.e., $0 < \zeta < 1$

$$\Delta_{\text{Model-3}}(r) = \frac{1}{(\varpi^2 + 0.75\varpi + 0.125)r^2} \times \left[0.5\varpi + \zeta^2\left(\varpi\left(\frac{0.65}{(\frac{r}{a_0})^{0.6}} - 0.5\right) + \frac{0.1625}{(\frac{r}{a_0})^{0.6}} - 0.125\right) + 0.125\right]. \tag{26}$$

Plotting anisotropy parameter $\Delta(r)$ versus r keeping throat radius fixed as $a_0 = 1$ and varying GMC parameter and correction parameter that has arisen from extra curvature terms due to $f(R, T)$ theory from Eqs. (24) to (26) are established in Fig. 6.

From the graphical analysis, it is observed that the anisotropy factor $\Delta(r)$ exhibits nontrivial behavior near the throat radius $r = a_0$. In particular, the regions $\Delta(r) > 0$ indicate an outward push due to tangential pressure dominance, thereby enhancing the stability of the WH structure. Figure 6 shows that for different varying values of all parameters taken into account, the anisotropy parameter $\Delta(r)$ results positive, illustrating that the geometry for the chosen specific WH model is repulsive in nature, making WH model more stable, i.e., in all panels (a) to (f) of Fig. 6, possessing repulsive geometry enabling the WH throat to be open as repulsion counteracts gravitational collapse. Thus, anisotropy emerges as a significant physical parameter in evaluating the stability and viability of GMC WHs in $f(R, T)$ gravity.

3.1 Energy conditions and WH models along with graphical evaluation

Energy conditions are mathematical guidelines that determine how matter and energy must behave in space-time, whereas according to GR, any EMT representing physically meaningful matter or energy should satisfy these conditions. Here are the Energy Conditions:

- Null Energy Condition (NEC): $\mu(r) \geq 0$ and $\mu(r) + p_i(r) \geq 0$, $\forall i \in \{1 = r, 2 = t\}$ for a fluid.
- Weak Energy Condition (WEC): $\mu(r) \geq 0$ and $\mu(r) + p_i(r) \geq 0$, $\forall i \in \{1 = r, 2 = t\}$ for a fluid. implies

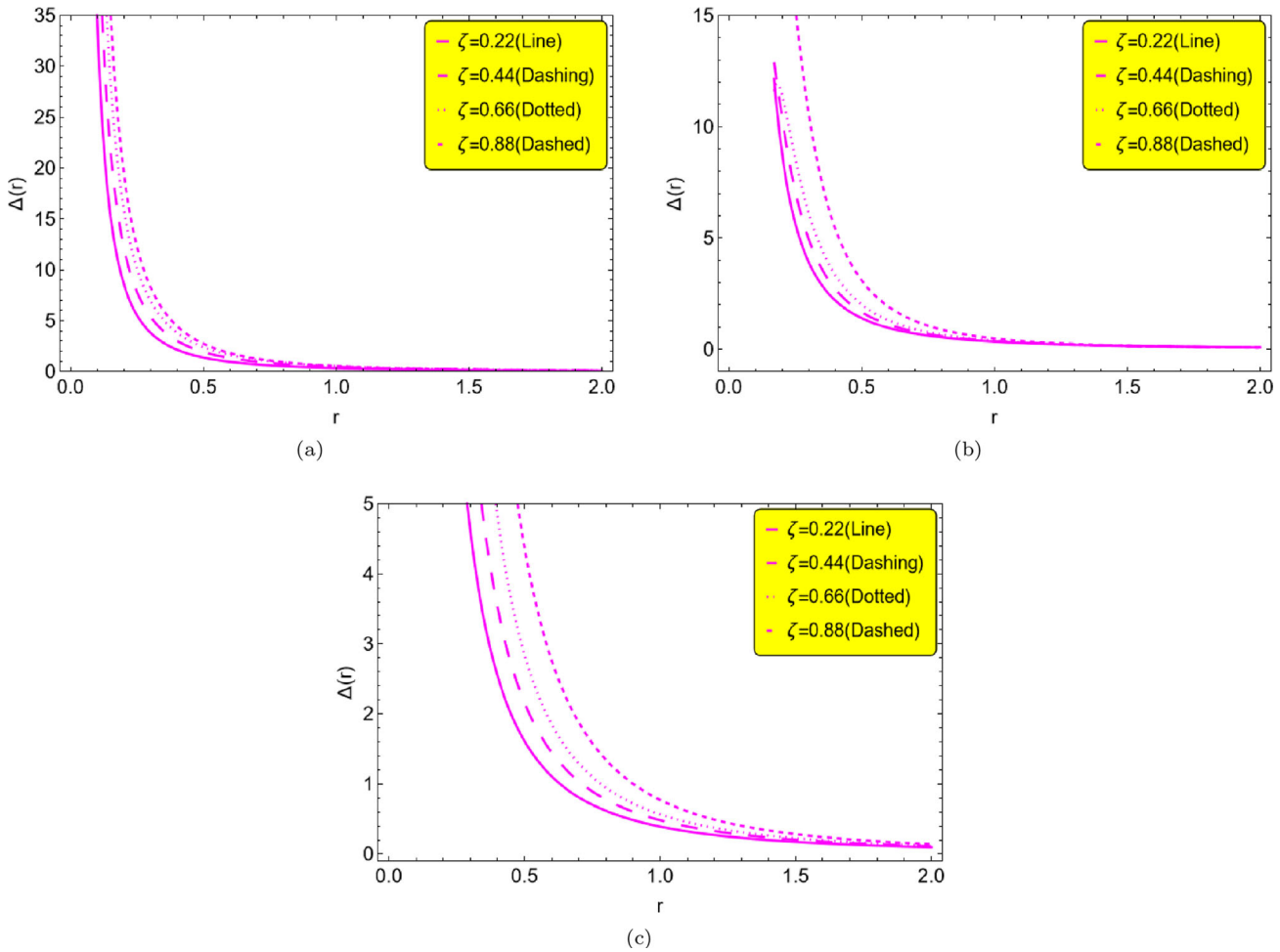

Fig. 6 Graphical representation of $\Delta(r)$ vs r with varying values of ζ, i.e., $0 < \zeta < 1$, throat radius $a_0 = 1$ and different values of correction parameter $0 < \varpi \leqslant 1$, panel (**a**) for model 1, panel (**b**) for model 2, and panel (**c**) for model 3, respectively

that the energy density measured by any observer is non-negative.

- Strong Energy Condition (SEC): $\mu(r)+p_i(r)+2p_j(r) \geq 0, \forall i, j \in \{1 = r, 2 = t\}$ for a fluid.
- Dominant Energy Condition (DEC): $\mu(r) - |p_i(r)| \geq 0$, $\forall i \in \{1 = r, 2 = t\}$ for a fluid. This means that energy flux cannot move faster than light.

These conditions are essential for ensuring the physically reasonable behavior of matter and energy in GR, and they play a critical role in singularity theorems and black hole physics, while WH requires these conditions' violations for traversability, as we have said earlier in the introduction of our article. These models are inspired by well-known functional forms in the literature, and for each case, the corresponding expressions for energy density and pressures are derived by substituting the shape function into the field equations. This allows us to evaluate the anisotropy parameter, which measures the difference between tangential and radial stresses, and to test the validity of classical energy conditions such as the NEC, WEC, SEC, and DEC. In addition, graphical analyses are employed to illustrate how the GMC and the matter geometry coupling parameter ϖ affect the physical behavior of these solutions.

3.2 Model-1: exponential shape function

We initiate our analysis of the WH geometry by adopting an exponential shape function, given by [106]:

$$A_1(r) = r\, e^{\gamma_1(a_0 - r)}, \tag{27}$$

where a_0 corresponds to the WH throat radius, the minimal radial coordinate at which the WH remains open, and γ_1 is a dimensionless parameter controlling the geometric profile of the WH. For simplicity in computation and without loss of generality, we set $a_0 = 1$. By substituting this shape function into the modified field equations Eqs. (13)–(15), we derive the key matter components supporting the WH structure: the

energy density μ, the radial pressure p_r, and the tangential pressure p_t. These quantities are obtained as follows:

$$\mu = \frac{(2\varpi-1)\left(\zeta^2\left((\gamma_1 r-1)e^{\gamma_1(a_0-r)}+1\right)-1\right)}{(4\varpi+1)r^2}, \tag{28}$$

$$p_r = \frac{-\left(\zeta^2\left(e^{\gamma_1(a_0-r)}\left(-4\varpi^2+4\gamma_1(\varpi+1)\varpi r+1\right)+4\varpi^2-1\right)\right)+4\varpi^2-1}{\left(8\varpi^2+6\varpi+1\right)r^2}, \tag{29}$$

$$p_t = -\frac{\zeta^2 e^{\gamma_1(a_0-r)}\left(\gamma_1\left(8\varpi^2+4\varpi-1\right)r-8\varpi(\varpi+1)\right)+8\left(\zeta^2-1\right)\varpi(\varpi+1)}{2\left(8\varpi^2+6\varpi+1\right)r^2}. \tag{30}$$

These expressions encode how the underlying matter-energy distribution behaves in response to both the chosen shape function and the MGT framework (through the coupling parameter ϖ and the GMC parameter ζ). The result (panel (a) of Fig. 7) highlights a significant departure from classical GR-based WH models, which generally require negative energy density. The $1/r^2$ dependence reflects the natural decay of matter density away from the throat. For the radial pressure p_r in Eq. (29), the numerator contains competing terms involving both r combined with ϖ, and a key feature required can be seen through panel (b) of Fig. 7. For the tangential pressure p_t in Eq. (30), the result remains positive for all considered parameter values, thus supplying lateral support against collapse (panel (c), Fig. 7). The combined effect of energy density, radial tension, and tangential pressure supports a physically consistent WH solution.

We next examine the classical energy conditions. The WECs take the form:

$$\mu + p_r = -\frac{\gamma_1\zeta^2 e^{\gamma_1(a_0-r)}}{2\varpi r + r}, \tag{31}$$

$$\mu + p_t = \frac{2-\zeta^2\left((\gamma_1 r-2)e^{\gamma_1(a_0-r)}+2\right)}{2(2\varpi+1)r^2}. \tag{32}$$

Here, $\mu + p_r$ corresponds to the radial WEC and $\mu + p_t$ to the tangential WEC. As shown in Fig. 8, the tangential WEC is satisfied, whereas the radial WEC is violated a common feature in traversable WH geometries.

The SEC computed as:

$$\mu + p_r + 2p_t = -\frac{8\varpi(\varpi+1)\left(\zeta^2\left((\gamma_1 r-1)e^{\gamma_1(a_0-r)}+1\right)-1\right)}{\left(8\varpi^2+6\varpi+1\right)r^2}. \tag{33}$$

Graphical analysis (Fig. 9) shows that SEC is satisfied for physically relevant parameter ranges, indicating that attractive gravity remains dominant.

The DECs for this model are:

$$\mu - |p_r| = \frac{\zeta^2\left(e^{\gamma_1(a_0-r)}\left(-8\varpi^2+\gamma_1\left(8\varpi^2+4\varpi-1\right)r+2\right)+8\varpi^2-2\right)-8\varpi^2+2}{\left(8\varpi^2+6\varpi+1\right)r^2}, \tag{34}$$

$$\mu - |p_t| = \frac{\zeta^2\left(e^{\gamma_1(a_0-r)}\left(-16\varpi^2-8\varpi+\gamma_1\left(16\varpi^2+4\varpi-3\right)r+2\right)+16\varpi^2+8\varpi-2\right)-16\varpi^2-8\varpi+2}{2\left(8\varpi^2+6\varpi+1\right)r^2}. \tag{35}$$

As depicted in Fig. 10, the radially directed DEC is satisfied, whereas the tangential DEC is violated again, reflecting anisotropic matter distribution.

3.3 Model-2: polynomial shape function

Now, we consider the following shape function [106]:

$$A_2(r) = a_0\left[\gamma_2\left(1-\frac{a_0}{r}\right)+1\right], \tag{36}$$

where γ_2 is a free parameter constrained within $0 < \gamma_2 < 1$ to ensure the satisfaction of the flare-out condition. Substituting Eq. (36) into the general field equations (13)–(15), the energy density μ, radial pressure p_r, and tangential pressure p_t are obtained as

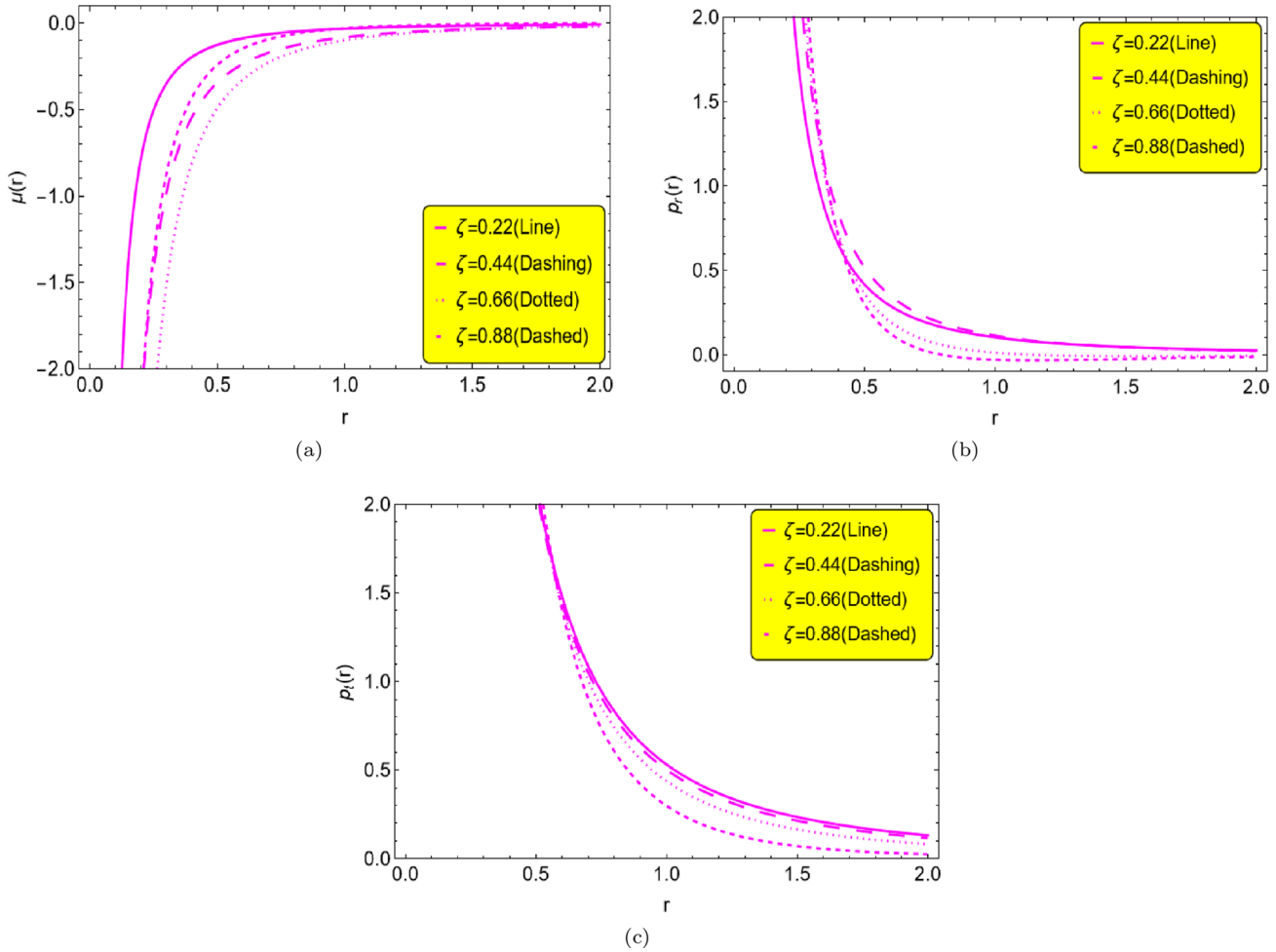

Fig. 7 Graphical representation of the first WH shape function $A(r) = r\, e^{\gamma_1(a_0-r)}$ for different values of GMC parameter $0 < \zeta < 1$, profiles of μ, p_r, and p_t in panels **a**, **b**, and **c**, respectively, as functions of r with $a_0 = 1$, and correction parameter $0 < \varpi \leq 1$

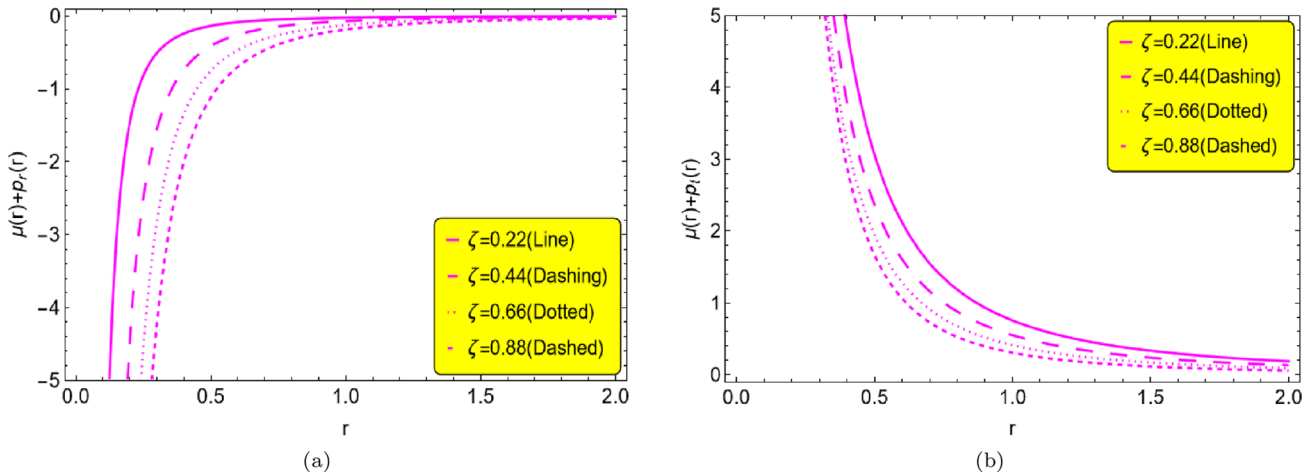

Fig. 8 Graphical representation of (16) and profiles of $\mu + p_r$ and $\mu + p_t$ in panels **a** and **b**, respectively, as functions of r for different values of $0 < \zeta < 1$, with $a_0 = 1$, and different values of correction parameter $0 < \varpi \leqslant 1$

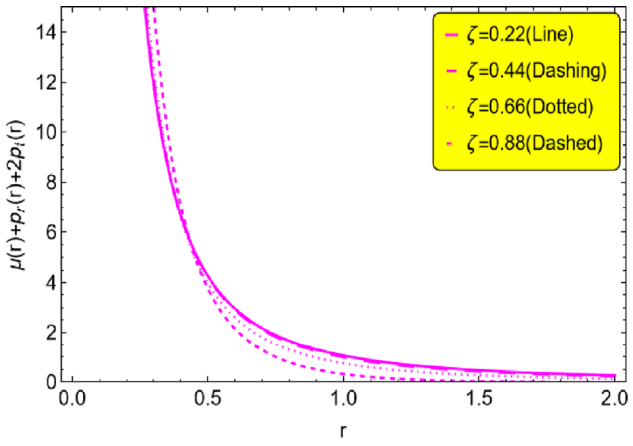

(a)

Fig. 9 Graphical behavior of $\mu + p_r + 2p_t$ versus r for different values of $0 < \zeta < 1$, with $a_0 = 1$, and different values of correction parameter $0 < \varpi \leqslant 1$

$$\mu = \frac{(2\varpi - 1)\left((\zeta^2 - 1)r^2 - \gamma_2\zeta^2 a_0^2\right)}{(4\varpi + 1)r^4}, \tag{37}$$

$$p_r = \frac{-(\zeta^2 - 1)(4\varpi^2 - 1)r^2 + \gamma_2\zeta^2(4\varpi^2 + 8\varpi + 1)a_0^2 - \left((\gamma_2 + 1)\zeta^2(4\varpi + 1)a_0 r\right)}{(8\varpi^2 + 6\varpi + 1)r^4}, \tag{38}$$

$$p_t = \frac{-8(\zeta^2 - 1)\varpi(\varpi + 1)r^2 + 2\gamma_2\zeta^2(4\varpi^2 - 1)a_0^2 + (\gamma_2 + 1)\zeta^2(4\varpi + 1)a_0 r}{2(8\varpi^2 + 6\varpi + 1)r^4}. \tag{39}$$

The graphical behavior of μ, p_r, and p_t is illustrated in Fig. 11. From these plots, we observe that the energy density μ is predominantly negative for most values of ζ and ϖ, indicating the requirement of EM contributions. On the other hand, both radial and tangential pressures remain positive for a significant range of parameter values, with the exception of very small ζ (e.g., $\zeta = 0.1$), where the radial pressure acquires a negative contribution. This indicates that the matter distribution associated with the chosen shape function is not completely exotic, but a partial violation of standard conditions still persists.

The WECs are derived from the above expressions as follows:

$$\mu + p_r = -\frac{\zeta^2 a_0(\gamma_2 r - 2\gamma_2 a_0 + r)}{(2\varpi + 1)r^4}, \tag{40}$$

$$\mu + p_t = \frac{(\gamma_2 + 1)\zeta^2 a_0 - 2(\zeta^2 - 1)r}{2(2\varpi + 1)r^3}. \tag{41}$$

The corresponding plots in Fig. 12 indicate that the WECs are satisfied for the considered parameter ranges, implying that despite the negative energy density, the combined fluid variables support physically admissible WH solutions under $f(R, T)$ gravity corrections.

For the SEC, we compute

$$\mu + p_r + 2p_t = -\frac{8\varpi(\varpi + 1)\left((\zeta^2 - 1)r^2 - \gamma_2\zeta^2 a_0^2\right)}{(8\varpi^2 + 6\varpi + 1)r^4}, \tag{42}$$

whose behavior is depicted in Fig. 13. The SEC is found to hold throughout the considered domain, confirming that the effective matter distribution under this shape function remains attractive.

Finally, the DECs take the forms

$$\mu - |p_r| = \frac{2(\zeta^2 - 1)(4\varpi^2 - 1)r^2 + (\gamma_2 + 1)\zeta^2(4\varpi + 1)a_0 r - 8\gamma_2\zeta^2\varpi(\varpi + 1)a_0^2}{(8\varpi^2 + 6\varpi + 1)r^4}, \tag{43}$$

$$\mu - |p_t| = \frac{2(\zeta^2 - 1)(8\varpi^2 + 4\varpi - 1)r^2 + 4\gamma_2\zeta^2(1 - 4\varpi^2)a_0^2 - (\gamma_2 + 1)\zeta^2(4\varpi + 1)a_0 r}{2(8\varpi^2 + 6\varpi + 1)r^4}. \tag{44}$$

The graphical results in Fig. 14 demonstrate that both radial and tangential DECs are violated, which suggests the breakdown of classical matter conditions. This violation is a direct consequence of higher-order curvature terms in $f(R, T)$ gravity, implying that the WH requires exotic-type contributions to remain traversable.

Thus we examine that this polynomial shape function illustrates a mixed scenario: although the WEC and SEC are largely respected, the DEC and negative energy density

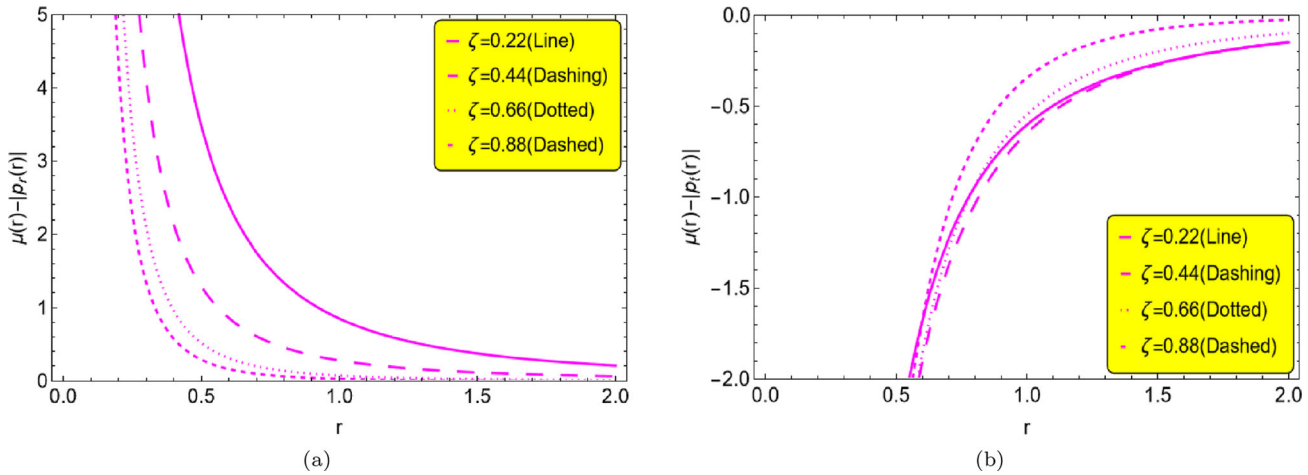

Fig. 10 Graphical representation of $\mu(r) - |p_r|$ and $\mu(r) - |p_t|$ in panels **a** and **b**, respectively, as functions of r for different values of $0 < \zeta < 1$, with $a_0 = 1$, and different values of correction parameter $0 < \varpi \leqslant 1$

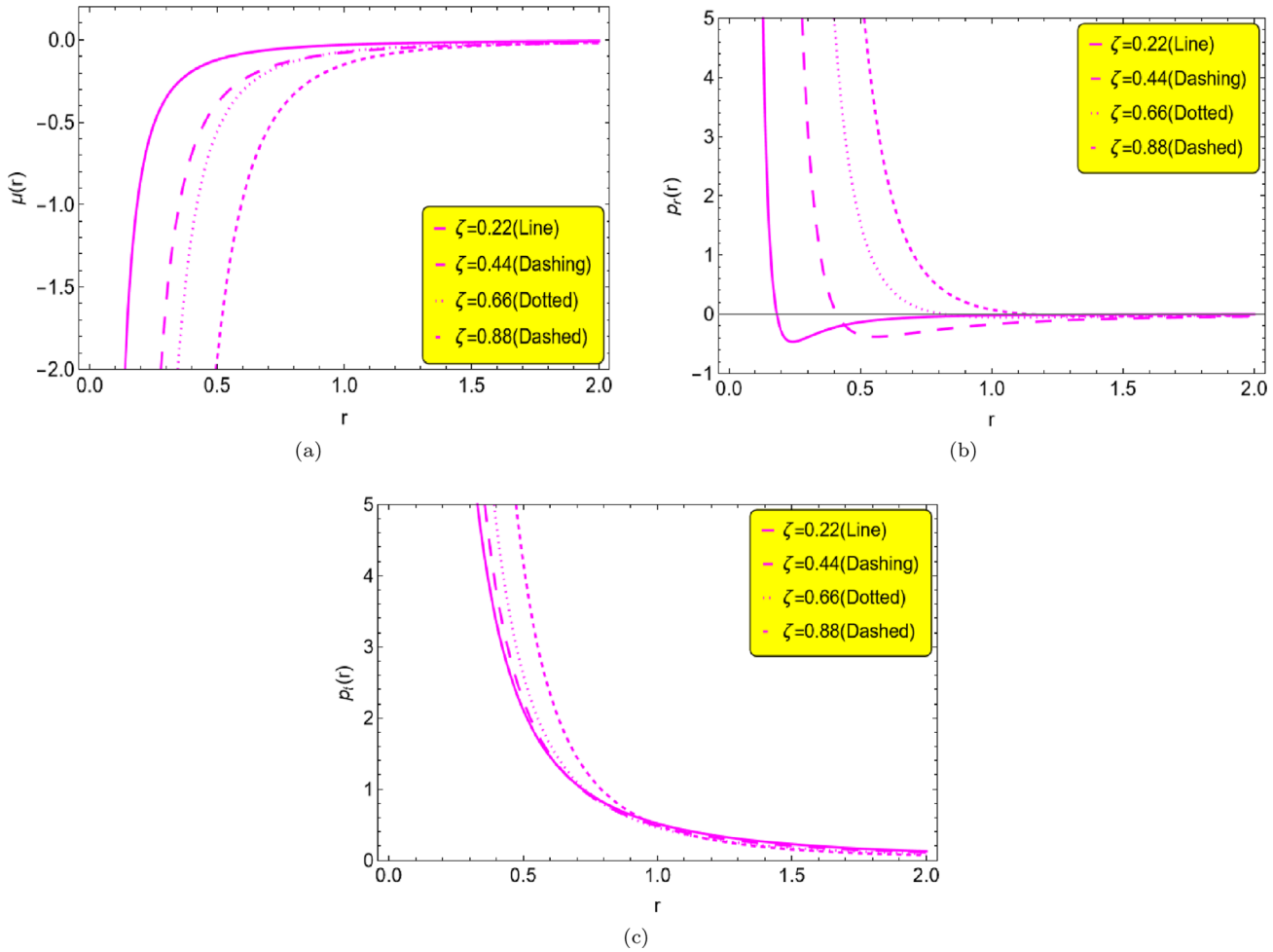

Fig. 11 Graphical representation of μ, p_r, and p_t in panels **a**, **b**, and **c**, respectively, as functions of r with varying values of ζ, i.e., $0 < \zeta < 1$, with throat radius $a_0 = 1$, $\gamma_2 = 0.1$, and correction parameter $0 < \varpi \leqslant 1$

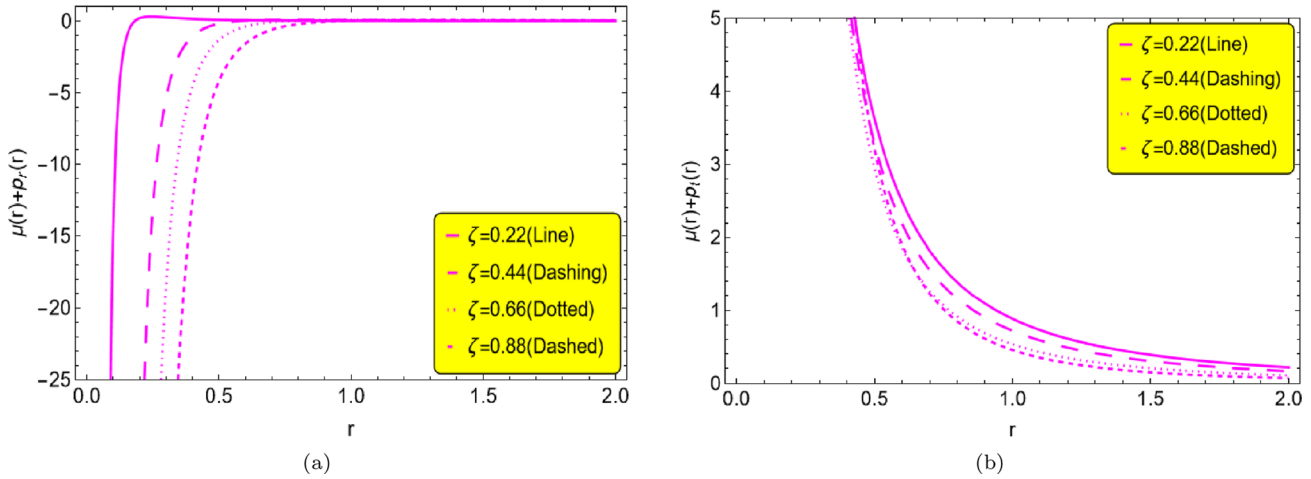

Fig. 12 Graphical representation of WECs, namely $\mu + p_r$ and $\mu + p_t$ in panels **a** and **b**, respectively, for different parameter choices with $a_0 = 1$, $\gamma_2 = 0.1$ and different values of correction parameter $0 < \varpi \leqslant 1$

indicate the persistence of exoticity in the matter sector. The incorporation of the correction parameter ϖ in $f(R, T)$ gravity plays a vital role in controlling these violations, yet does not completely eliminate them. Thus, the WH solutions supported by this shape function are only partially non-exotic, with the overall geometry favoring repulsive contributions due to the presence of GMC.

3.4 Model-3: power-law shape function

In this model, we adopt the following expression for the shape function [107].

$$A_3(r) = a_0\left(\frac{r}{a_0}\right)^{\gamma_3}, \quad 0 < \gamma_3 < 1, \tag{45}$$

where a_0 is the throat radius, γ_3 is an arbitrary constant with the restriction $0 < \gamma_3 < 1$ to satisfy the flaring out condition. We have made calculations for the value of $\gamma_3 = 0.4$. Utilizing this value of γ_3 and expression of shape function, we have found expressions for energy density, radial pressure, and tangential pressure as below:

$$\mu = \frac{1}{(4\varpi+1)r^2}\left[(2\varpi-1)\left(0.4\zeta^2\left(\frac{r}{a_0}\right)^{-0.6} - \zeta^2 + 1\right)\right], \tag{46}$$

$$p_r = -\frac{1}{\left(8\varpi^2+6\varpi+1\right)r^3} \times \left[\left(\zeta^2-1\right)\left(4\varpi^2-1\right)r + \zeta^2(4\varpi+1) \times \left(\frac{r}{a_0}\right)^{0.4}a_0 - \left(1.6\zeta^2\varpi(\varpi+1)r\right)\left(\frac{r}{a_0}\right)^{-0.6}\right], \tag{47}$$

$$p_t = \frac{1}{2\left(8\varpi^2+6\varpi+1\right)r^3} \times \left[\left(0.4\zeta^2\left(8\varpi^2+4\varpi-1\right)r\right)\left(\frac{r}{a_0}\right)^{-0.6} + \zeta^2(4\varpi+1) \times \left(\frac{r}{a_0}\right)^{0.4}a_0 - 8\left(\zeta^2-1\right)\varpi(\varpi+1)r\right]. \tag{48}$$

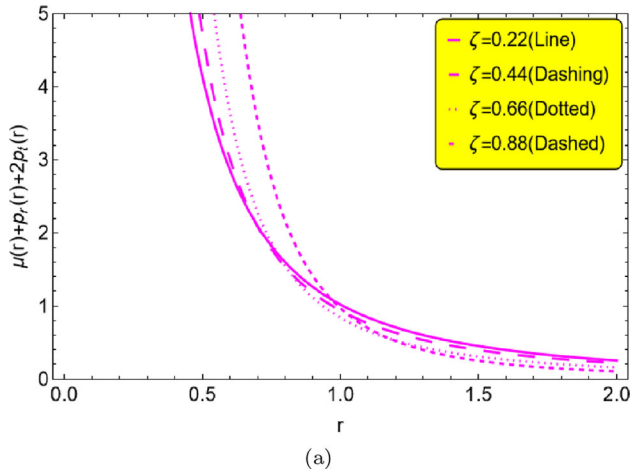

Fig. 13 Graph of the SEC, i.e., $\mu + p_r + 2p_t$, versus r for chosen parameter values with throat radius $a_0 = 1$, $\gamma_2 = 0.1$ and different values of correction parameter $0 < \varpi \leqslant 1$

Now, from Eq. (46), the energy density is inversely proportional to r^2, a typical feature in spherically symmetric systems, indicating that energy density peaks near the WH throat and decreases outward. Whereas a negative power term, reflecting corrections due to the matter-geometry coupling in $f(R, T)$ gravity. The overall negative sign indicates that it often becomes negative, representing radial tension a crucial feature needed to keep a WH throat open and a common indicator of the presence of EM. Similarly, the tangential pressure equation turns out to be positive throughout.

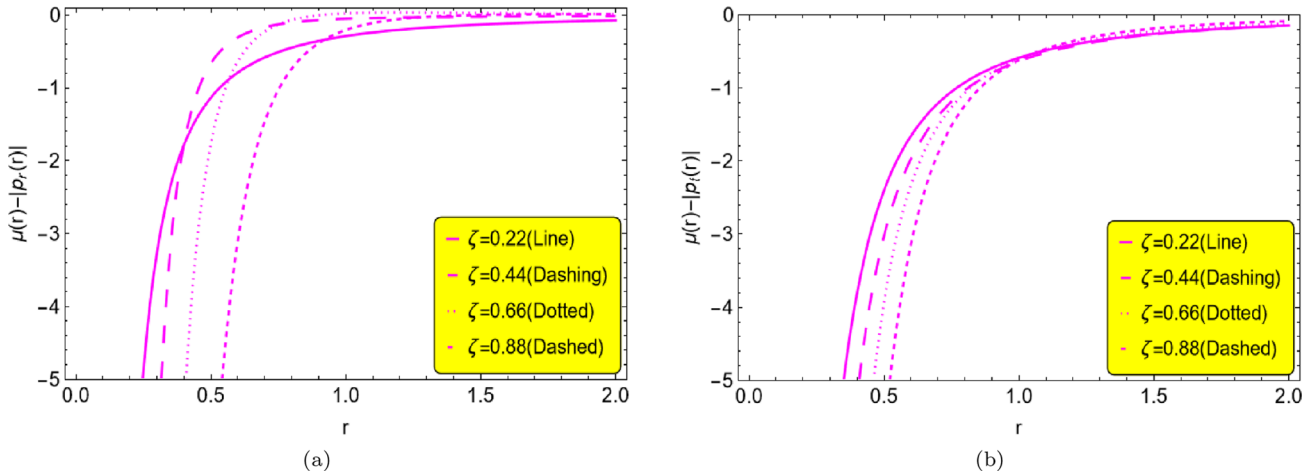

Fig. 14 Graphical representation of $\mu - |p_r|$ and $\mu - |p_t|$ in panels **a** and **b**, respectively, for different parameter choices with $a_0 = 1$, $\gamma_2 = 0.1$ and different values of correction parameter $0 < \varpi \leqslant 1$

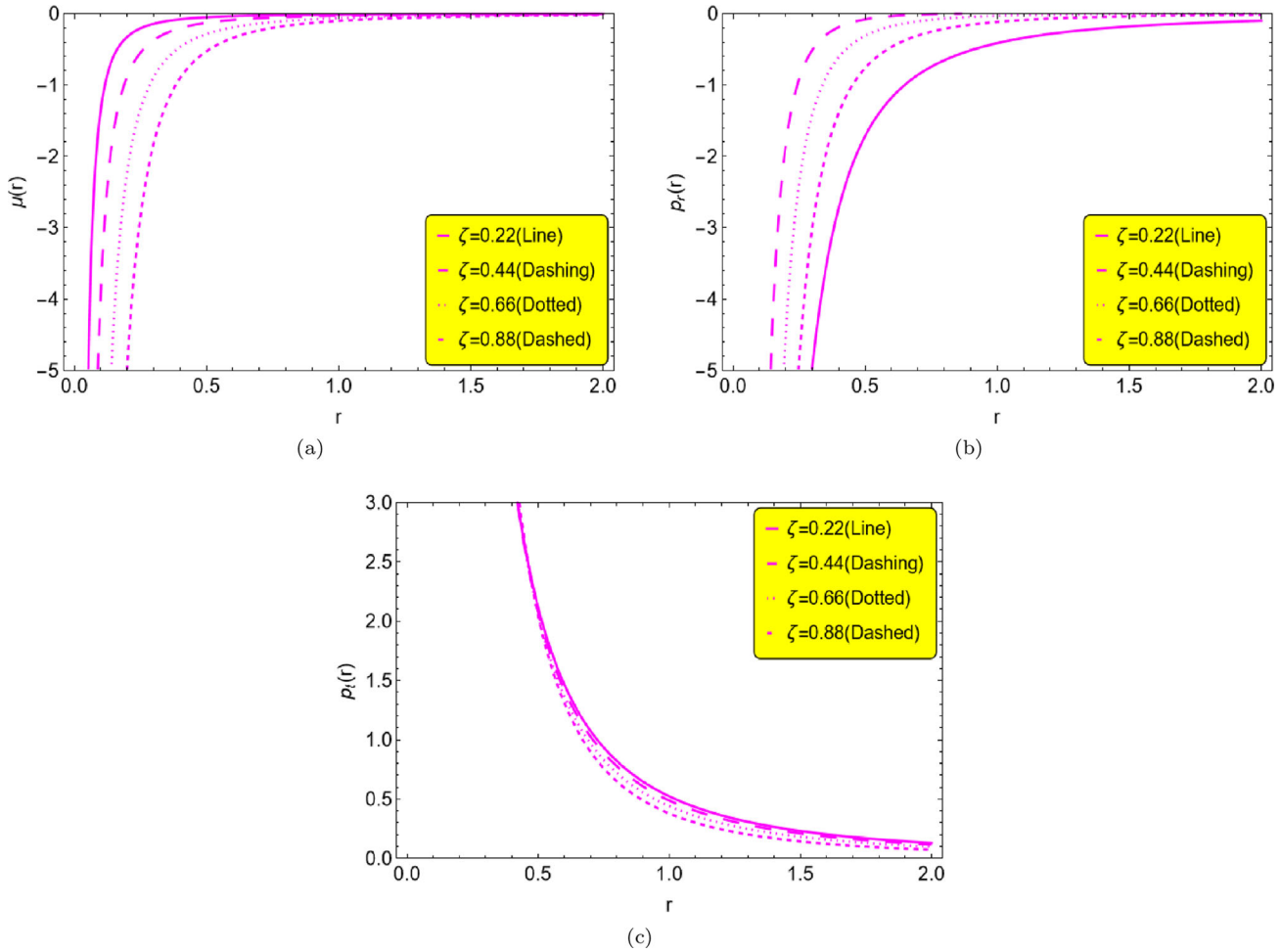

Fig. 15 Pictorial representation of μ, p_r, p_t in panels **a**, **b** and **c**, respectively, as function of r with varying values of ζ, i.e., $0 < \zeta < 1$, throat radius $a_0 = 1$ and different values of correction parameter $0 < \varpi \leqslant 1$

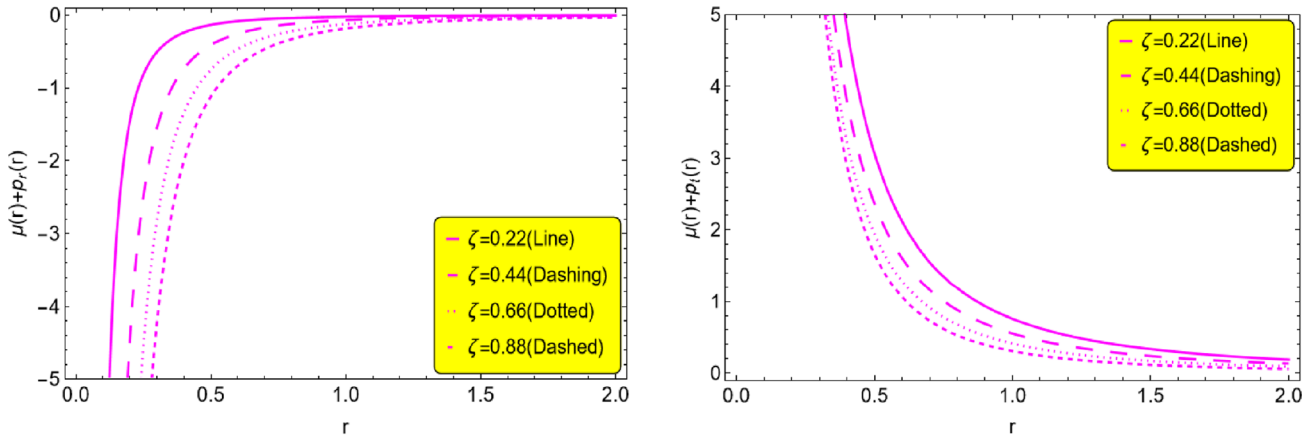

Fig. 16 Pictorial representation of $\mu + p_r$, $\mu + p_t$, in panels **a**, **b**, respectively, as a function of r with varying values of ζ, i.e., $0 < \zeta < 1$, throat radius $a_0 = 1$ and different values of correction parameter $0 < \varpi \leqslant 1$

In this analysis, we present a set of graphs illustrating the energy density, radial pressure, and tangential pressure with respect to r, while maintaining a fixed throat radius $a_0 = 1$ and varying different values of GMC parameter ζ. It is observed that the energy density of the anisotropic fluid remains negative except for $\zeta = 0.1$. The next graphs show up tangential pressure positive and radial pressure negative for all values of GMC parameter ζ and correction parameter ϖ (Fig. 15).

The WECs imply that:

$$\mu + p_r = -\frac{1}{(\varpi + 0.5)r^2}\left[0.3\zeta^2\left(\frac{r}{a_0}\right)^{-0.6}\right], \tag{49}$$

$$\mu + p_t = \frac{1}{(\varpi + 1)r^2}\left[\zeta^2\left(0.7\left(\frac{r}{a_0}\right)^{-0.6} - 1\right) + 1\right]. \tag{50}$$

The set of plots for WECs is given below:

And the graphical representation of WECs in Fig. 16 illustrates that radial directed is violated totally and tangential directed is held true for the model under investigation. The SEC implies that:

$$\mu + p_r + 2p_t = \frac{1}{(\varpi^2 + 0.75\varpi + 0.125)r^2} \times \left[\varpi\left(\varpi + \zeta^2\left(\varpi\left(\frac{0.4}{\left(\frac{r}{a_0}\right)^{0.6}} - 1\right) + \frac{0.4}{\left(\frac{r}{a_0}\right)^{0.6}} - 1\right) + 1\right)\right]. \tag{51}$$

The graph for SEC is plotted below, which indicates that in the model under investigation, SEC has been satisfied for all values of GMC parameter ζ and correction parameter ϖ (Fig. 17). The DECs imply that:

$$\mu - |p_r| = \frac{1}{(8\varpi^2 + 6\varpi + 1)r^2}\left(\frac{r}{a_0}\right)^{-0.6}$$

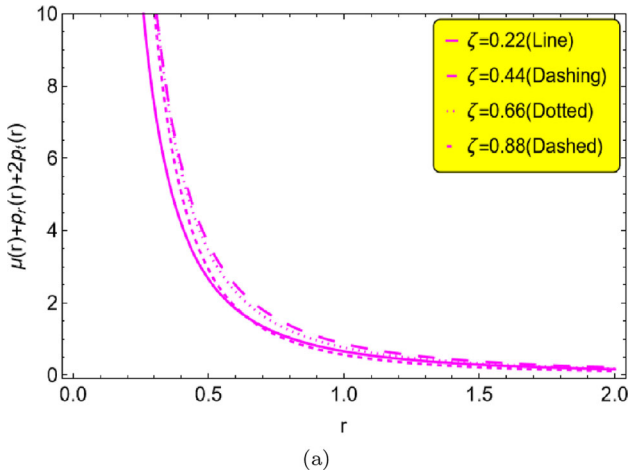

Fig. 17 Graph for SEC, i.e., $\mu + p_r + 2p_t$ versus r with varying values of ζ, i.e., $0 < \zeta < 1$, throat radius $a_0 = 1$ and different values of correction parameter $0 < \varpi \leqslant 1$

$$\times \left[\left(\frac{r}{a_0}\right)^{0.6}(2 - 8\varpi^2) + \zeta^2(2.4\varpi + \varpi^2(8\left(\frac{r}{a_0}\right)^{0.6} - 3.2) - 2\left(\frac{r}{a_0}\right)^{0.6} + 1.4)\right], \tag{52}$$

$$\mu - |p_t| = \frac{1}{(8\varpi^2 + 6\varpi + 1)r^2} \times \left[\zeta^2(\varpi^2(8 - \frac{3.2}{\left(\frac{r}{a_0}\right)^{0.6}}) + \varpi(4 - \frac{2.8}{\left(\frac{r}{a_0}\right)^{0.6}}) + \frac{0.1}{\left(\frac{r}{a_0}\right)^{0.6}} - 1) - 8\varpi^2 - 4\varpi + 1\right]. \tag{53}$$

The graphs for DECs are given below in Fig. 18.

The graphs drawn above illustrate the violation of tangentially directed DEC, suggesting unusual energy conditions or exotic stuff due to extra curvature terms arising from our underlying $f(R, T)$ theory.

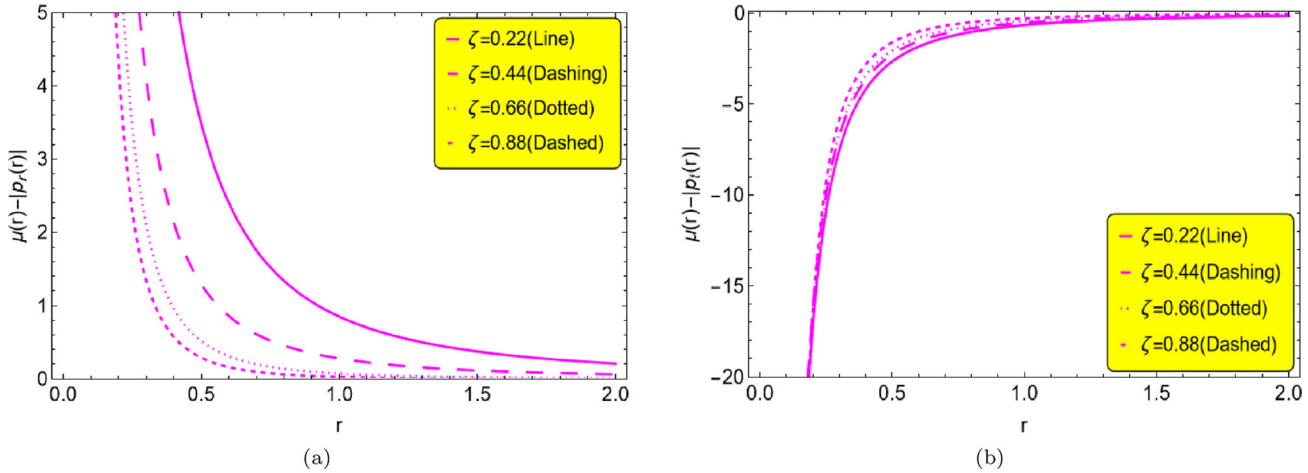

Fig. 18 Pictorial representation of $\mu(r) - |p_r|$, $\mu(r) - |p_t|$, in panels **a**, **b**, respectively, as function of r with varying values of ζ, i.e., $0 < \zeta < 1$, throat radius $a_0 = 1$ and different values of correction parameter $0 < \varpi \leqslant 1$

3.5 VIQ and comparative EM analysis in WH models

The existence of traversable WH geometries necessitates the presence of EM, which is characterized by a violation of the NEC, i.e., $\mu + p_r < 0$, where μ is the energy density and p_r the radial pressure, while this violation is crucial as it counteracts the gravitational collapse of the WH throat, thereby ensuring the stability and structural integrity of the WH. To quantitatively assess the total amount of EM content within a WH configuration, the VIQ serves as a powerful diagnostic tool that measures the degree of NEC violation integrated over the entire spatial volume of the WH. Mathematically, it is defined as:

$$VIQ(r) = \oint (\mu(r) + p_r(r))\, dV, \tag{54}$$

where $dV = r^2 dr d\Omega$ denotes the proper volume element and $d\Omega$ represents the solid angle element, whereas given the spherical symmetry of the configuration, the integral over the solid angle yields 4π, and the expression simplifies to: $VIQ(r) = \int_{a_0}^{\infty} 4\pi\, (\mu(r) + p_r(r))\, r^2 dr$. However, to obtain a finite measure and restrict the analysis to a physically meaningful region surrounding the WH throat, the integration is performed from the throat radius a_0 up to a finite upper bound $R_1 \geq a_0$. This practical form of the VIQ is given by:

$$VIQ(r) = \int_{a_0}^{R_1} 4\pi\, (\mu(r) + p_r(r))\, r^2 dr. \tag{55}$$

In our study, we employ Eq. (55) to evaluate the VIQ for the considered WH models featuring different shape functions. For our numerical computations, the throat radius is fixed at $a_0 = 1$, and R_1 is chosen as a suitable finite upper limit. The resulting distributions and parameter dependencies of the EM are graphically illustrated in all the panels of Figs. 19, 20, and 21, providing a comprehensive visualization of the NEC violation across the parameter space of our solutions. These figures illustrate the computed VIQ profiles as functions of the radial coordinate r for the three shape function models under consideration. The curves are plotted for parameter sets $\varpi \in \{0.25, 0.5, 0.75\}$, representing the correction parameter in the $f(R, T)$ gravity model, and $\zeta \in \{0.3, 0.6, 0.9\}$, GMC parameter, while fixing throat radius $a_0 = 1$ and for some shape function parameters, i.e., (in Fig. 19, $\gamma_1 = 0.5$, in Fig. 20, $\gamma_2 = 0.5$ and in Fig. 21, $\gamma_3 = 0.4$).

As shown in nine panels of Fig. 19, the VIQ generally decreases with increasing r, reflecting the cumulative negative contribution of EM, while larger values of ϖ and ζ tend to amplify the magnitude of VIQ, indicating increased amounts of EM necessary to sustain the WH geometry. Notably, the VIQ curves exhibit a steeper decline near the throat ($r = a_0$), suggesting that most EM is concentrated in the vicinity of the throat region. Consequently, we can say that the parameter combinations with lower ϖ and ζ, throat radius $a_0 = 1$, and shape function parameter $\gamma_1 = 0.5$, maintain VIQ values closer to zero, implying physically more viable WH solutions with minimal EM.

In contrast, all the panels of our constructed 2D visualization in Fig. 20 displays a distinct VIQ behavior influenced by the polynomial form of the shape function, here, the dependence on parameters ϖ, ζ, throat radius $a_0 = 1$ and shape function parameter $\gamma_2 = 0.5$, influences the VIQ magnitude in a more delicate and gradual way. It means that the impact of changing these parameters on the total EM content (measured by VIQ) is more gentle, less intense, and less easily detected compared to other cases where the variations cause larger or more noticeable changes. The VIQ curves tend to level off more gradually compared to Model 1, suggesting a

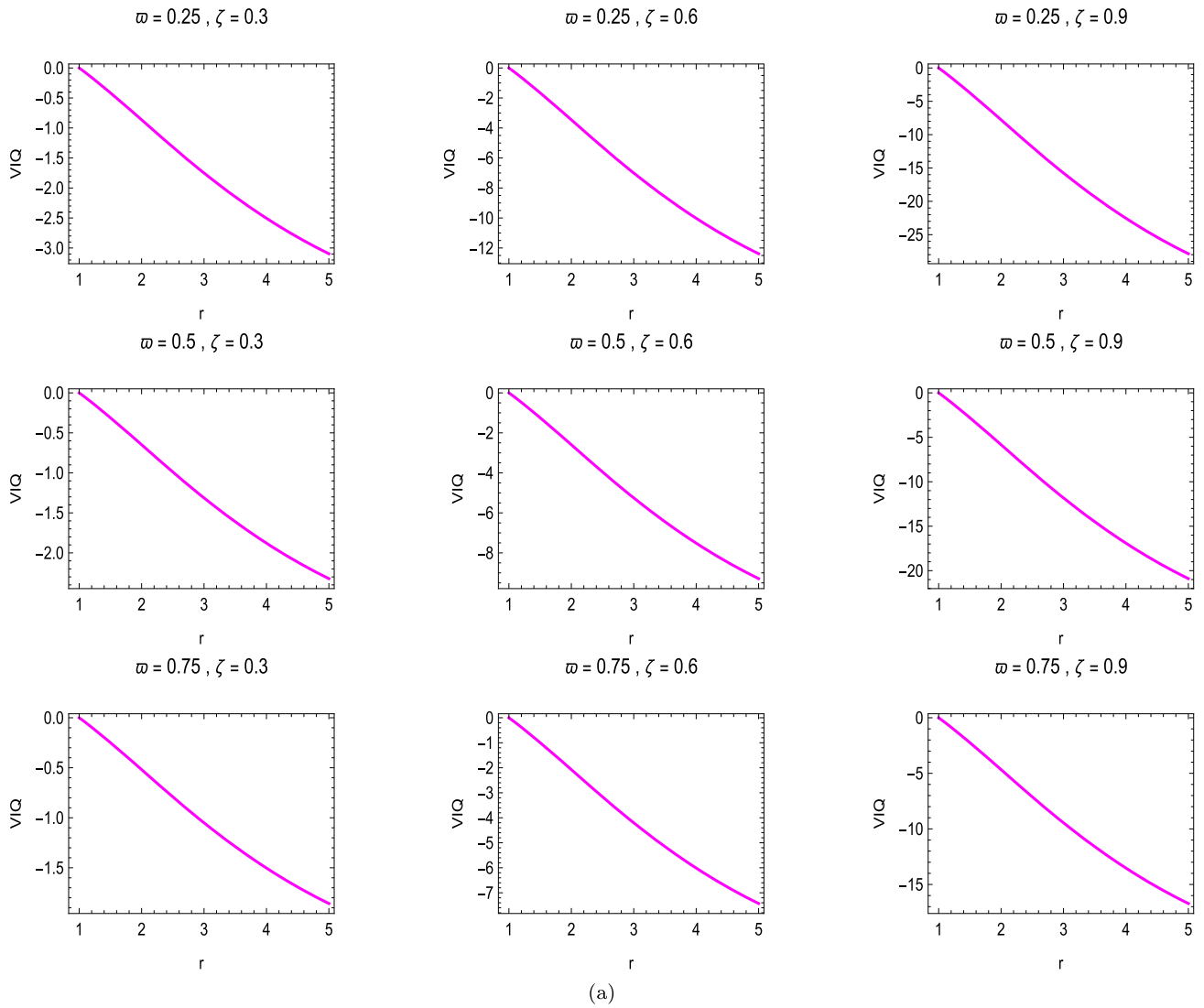

Fig. 19 2D visualization for VIQ versus radial coordinate r for Model 1 shape function with varying of correction parameter $0 < \varpi \leqslant 1$ and GMC parameter $0 < \zeta < 1$, respectively, as VIQ quantifies the total EM content supporting the WH geometry, throat radius $a_0 = 1$ and shape function parameter $\gamma_1 = 0.5$

wider spatial distribution of EM, interestingly, certain parameter choices result in a less negative VIQ profile, indicating reduced EM content for this shape function model. This highlights the important role that the functional form of the shape function plays in determining EM requirements.

The 2D visualization in Fig. 21 reveals the VIQ behavior for the power-law shape function where additional powers of r affect the density and pressure profiles, where as the effect of varying ϖ and ζ, also the radius of the throat $a_0 = 1$ and the shape function parameter $\gamma_3 = 0.4$ is somewhat intermediate between the previous two models. The VIQ curves demonstrate smooth variations with r, and higher values of the correction parameter ϖ consistently lead to higher negative VIQ values, suggesting an increase in EM. Here, the power-law nature slightly broadens the EM region compared to the exponential model but concentrates it more than the polynomial model, while the comparative analysis confirms that all three shape functions require EM distributed around the WH throat, with the total amount quantified by the VIQ. We can examine that Model 1 generally demands the highest concentration of EM near the throat, while Model 2 exhibits a broader and somewhat reduced EM distribution, where as Model 3 provides intermediate behavior, balancing locality and spread of EM. Consequently, the dependence of VIQ on the parameters ϖ and ζ underscores the intricate interplay between the effects of MGT and topological defects such as GMC, influencing the physical possibility of WH configurations. So, smaller values ϖ and ζ are preferred to minimize EM content, improving the feasibility of stable

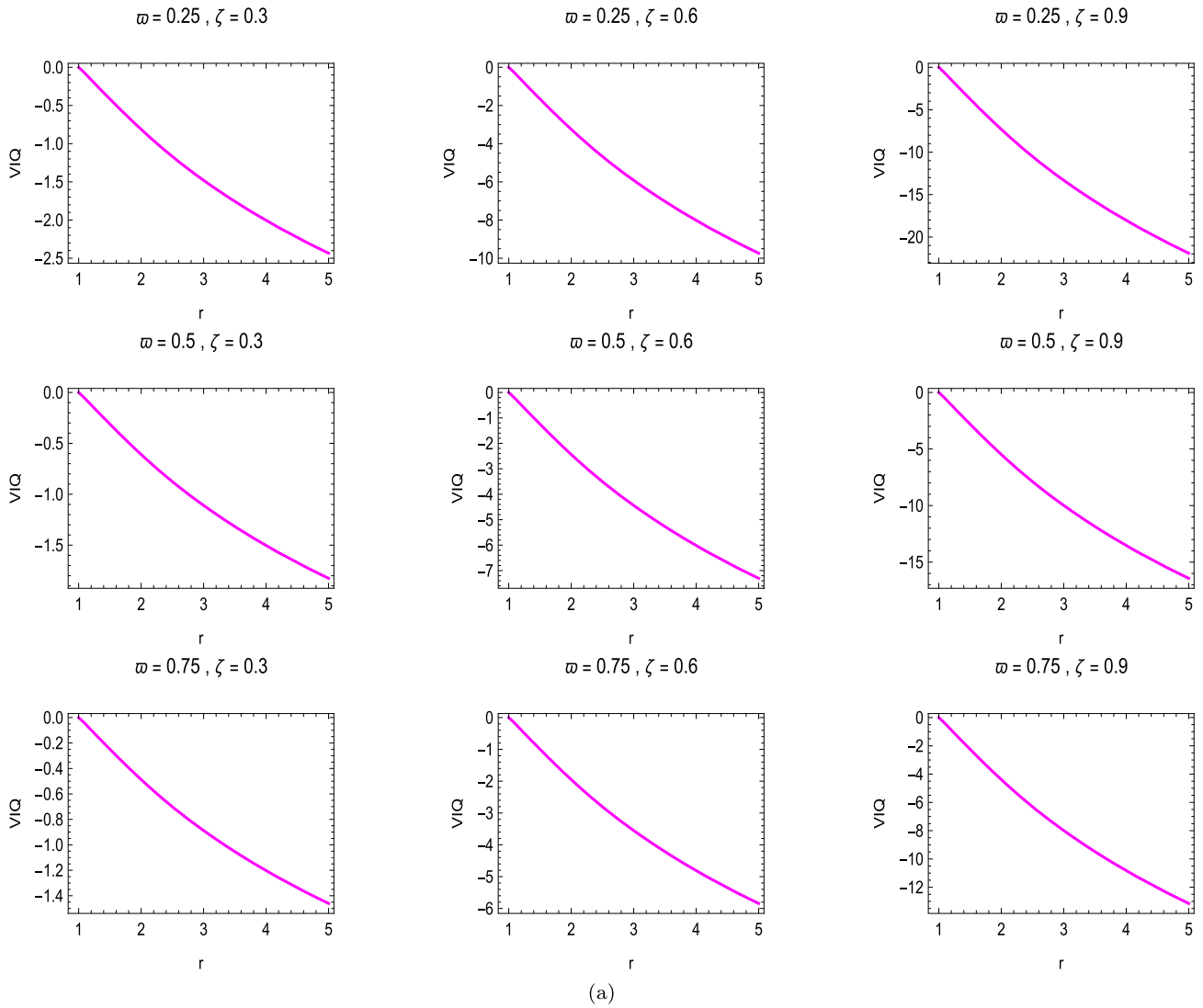

Fig. 20 VIQ versus r for Model 2 shape function with different variations of correction parameter $0 < \varpi \leqslant 1$ and GMC parameter $0 < \zeta < 1$, respectively, throat radius $a_0 = 1$ and shape function parameter $\gamma_2 = 0.5$

and traversable WHs in the background of our considered $f(R, T)$ gravitational frameworks.

4 Summary of work

The existence of traversable WHs (Morris–Thorne WHs) in GR is contingent upon the violation of the energy requirements. In GR, it is difficult to find precise solutions that characterize WHs, particularly when one wants to include a particular equation of state. The WHs are predicted to exist by a number of gravity theories, much like black holes, despite the fact that there is currently no direct observable proof of them, while it is still crucial to investigate WHs since a better knowledge of their characteristics may one day aid in their detection. It was widely held that the existence of EM was essential to the maintenance of a traversable WH; however, as the introduction section explains, some researchers have effectively created static, spherically symmetric WH models that do not require EM in both GR and MGT frameworks.

In this article, we have inspected topologically charged Morris–Thorne-type WHs against the backdrop of modified $f(R, T)$ theory employing various shape functions available in the literature with an anisotropic fluid as the matter content. Our analysis of three illustrative WH shape function models confirms that all satisfy the fundamental flare-out conditions and asymptotic flatness requirements essential for constructing traversable WHs; consequently, the graphical representations of these shape functions are provided in Figs. 1, 2, and 3 The embedding representations reveal the expected vertical slope at the throat and gradual flattening at large radii, providing a consistent geometric realization of the WH structures.

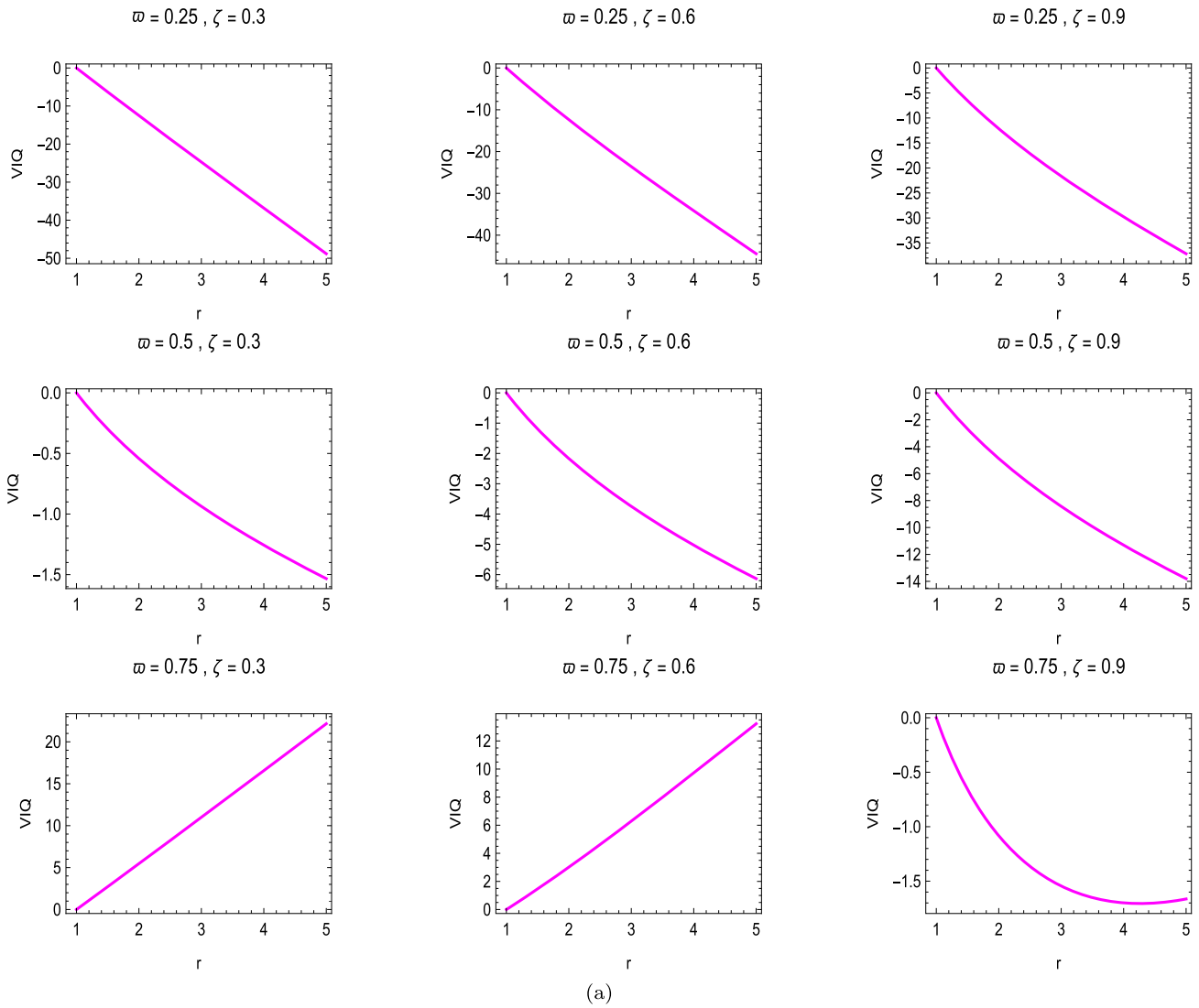

Fig. 21 Graphs for VIQ versus r by taking Model 3 shape function highlighting intermediate EM localization with varying values of ζ, i.e., $0 < \zeta < 1$, throat radius $a_0 = 1$ with varying values of correction parameter $0 < \varpi \leqslant 1$

The model parameters $(\gamma_1, \gamma_2, \gamma_3)$ and GMC parameter ζ play crucial roles in shaping the curvature and controlling the throat size, with higher ζ leading to wider throats and smoother curvature profiles, co.Consequently, we can say this governs the z-profile of the embedded WH surface, while the embedding diagrams corresponding to $A_1(r)$, $A_2(r)$, and $A_3(r)$ are presented in Figs. 4 and 5. Collectively, these findings establish that the considered models produce physically viable WH geometries supported within the adopted MGT framework. We solve the Einstein field equations to assess physical quantities such as energy density, radial pressure, tangential pressure, and weak, strong, and DECs in various models. This conclusion results from the observation that the matter content indicated by the effective stress–energy tensor relaxes the conventional requirements for EM in such configurations by violating certain energy conditions. Furthermore, our results show that the GMC, defined by the parameter ζ, is key in determining the energy requirements and that the WH geometry is supported by correction terms that are triggered by the modified structure formalism of the theory $f(R, T)$. The GMC parameter ζ and the relativistic correction parameter ϖ determine whether the WH's geometry shows attractive or repulsive behavior, affecting WH stability. This is additionally demonstrated by examining the anisotropy parameter for all models.

We also analyzed that the anisotropy factor $\Delta(r) = p_t - p_r$ for the WH configurations charged with monopoles considered in the framework of $f(R, T)$ gravity reveals several important results. The anisotropy parameter $\Delta(r)$ is found to be predominantly positive for all three shape function models considered, with varying choices of GMC parameter $0 < \zeta < 1$ and the correction parameter $0 < \varpi \leqslant 1$.

Therefore, anisotropy emerges as a key physical mechanism in sustaining traversable WHs in $f(R, T)$ gravity, with GMC and gravity model corrections working jointly to strengthen stability. Among these three models, the exponential shape function generally demands the highest concentration of EM near the throat. The second toy form of the shape function, which is a polynomial shape function, distributes EM more broadly and with subtler dependence on gravity and GMC parameters. Whereas the power-law shape function serves as an intermediate case, balancing EM localization and spread. Moreover, we investigated that variation of the $f(R, T)$ correction parameter and GMC parameter, along with $a_0 = 1$the significant modulation of the amount of EM, which is supported graphically through Figs. 19, 20 and 21. Hence, this research makes a substantial contribution to the continuing exploration of the theoretical viability and potential consequences of these intriguing space-time pathways, particularly when considering the influence of a GMC and taking the modified theory into account.

Funding No Funding.

Data Availability Statement This manuscript has no associated data. [Author's comment: The current article is just theoretical article. We can share calculations on reasonable requests.]

Code Availability Statement This manuscript has no associated-code/software. [Author's comment: Code/Software sharing not applicable to this article as no code/software was generated oranalysed during the current study while the plot and other calculations are performed using Mathematica. However this work hasalready included a comprehensive analysis and the corresponding calculations.]

Declarations

Conflict of interest The authors declare that they have no known competing financial interests or personal relationships that could have appeared to influence the work reported in this paper.

Funded by SCOAP[3].

References

1. A. Einstein et al., Ann. Phys. **17**(10), 891 (1905)
2. A. Einstein, Akad. Wiss. **47**(2), 831–839 (1915)
3. G. Lemaître, Proc. Natl. Acad. Sci. **20**(1), 12 (1934)
4. J.C. Niemeyer, K. Jedamzik, Phys. Rev. D **59**(12), 124013 (1999)
5. K.S. Thorne, Rev. Mod. Phys. **52**(2), 285 (1980)
6. P. Anninos, Living Rev. Relativ. **4**(1), 2 (2001)
7. D.J. Eisenstein, I. Zehavi, D.W. Hogg, R. Scoccimarro, M.R. Blanton, R.C. Nichol, R. Scranton, H.-J. Seo, M. Tegmark, Z. Zheng et al., Astrophys. J. **633**(2), 560 (2005)
8. B. Leibundgut, Astron. Astrophys. Rev. **10**, 179 (2000)
9. L. Östman, E. Mörtsell, J. Cosmol. Astropart. Phys. **2005**(02), 005 (2005)
10. P.A. Ade, N. Aghanim, M. Arnaud, M. Ashdown, J. Aumont, C. Baccigalupi, A. Banday, R. Barreiro, J. Bartlett, N. Bartolo et al., Astron. Astrophys. **594**, A13 (2016)
11. J.A. Frieman, M.S. Turner, D. Huterer, Annu. Rev. Astron. Astrophys. **46**(1), 385 (2008)
12. M.J. Mortonson, D.H. Weinberg, M. White (2013). arXiv:1401.0046
13. P. Brax, Rep. Prog. Phys. **81**(1), 016902 (2017)
14. M.Z. Gul, M. Sharif, I. Hashim, Phys. Dark Universe **45**, 101537 (2024)
15. Z. Yousaf, Phys. Dark Universe **48**, 101884 (2025)
16. R. Arnowitt, S. Deser, C. Misner, Ann. Phys. **33**, 88 (1965)
17. S. Capozziello, V.F. Cardone, E. Piedipalumbo, C. Rubano, Class. Quantum Gravity **23**(4), 1205 (2006)
18. K. Bamba, et al., Astrophys. Space Sci. **342**, 155 (2012)
19. S. Capozziello, M. De Laurentis, Phys. Rep. **509**, 167 (2011)
20. S. Nojiri, S.D. Odintsov, Phys. Rep. **505**, 59 (2011)
21. T. Clifton, P.G. Ferreira, A. Padilla, C. Skordis, Phys. Rep. **513**, 1 (2012)
22. S. Nojiri, S.D. Odintsov, Mod. Phys. Lett. A **29**, 1450211 (2014)
23. S. Nojiri, S. Odintsov, V. Oikonomou, Phys. Rep. **692**, 1 (2017)
24. M.Z. Bhatti, M. Yousaf, Z. Yousaf, Gen. Relativ. Gravit. **55**, 16 (2023)
25. V.A. Derkach, C. Trunk, J.R. Yusupov, D.U. Matrasulov, J. Phys. A: Math. Theor. **58**(34), 345201 (2025)
26. B. Turimov, S. Usanov, Y. Khamroev, Phys. Dark Universe **48**, 101876 (2025)
27. M.M. Suleimanov, M.U. Nosirov, H.T. Yusupov, A. Chaves, G. Berdiyorov, K.Y. Rakhimov, Phys. B: Condens. Matter **714**, 417484 (2025)
28. M. Zahid, Ch. Shen, J. Rayimbaev, B. Rahmatov, I. Ibragimov, S. Muminov, M. Umaraliyev, Phys. Dark Universe **50**, 102124 (2025)
29. K. Myrzakulov, O. Donmez, M. Koussour, S. Muminov, E. Davletov, J. Rayimbaev, Phys. Lett. A **534**, 130232 (2025)
30. H. Asad, M. Yousaf, B. Almutairi, L. Zahid, A.S. Khan, Phys. Dark Universe **46**, 101666 (2024)
31. M. Yousaf, Chin. J. Phys. **95**, 1278 (2025)
32. M.Z. Gul, M. Sharif, A. Arooj, Fortschr. Phys. **72**, 2300221 (2024)
33. A. Rehman, T. Naseer, B. Dayanandan, Nucl. Phys. B **1013**, 116852 (2025)
34. T. Naseer, M. Sharif, Eur. Phys. J. C **84**, 554 (2024)
35. M.M.M. Nasir, M.Z. Gul, O. Donmez, F. Javed, B. Almutairi, Eur. Phys. J. C **85**, 189 (2025)
36. T. Naseer, A. Rehman, M. Sharif, N. Alessa, A.-H. Abdel-Aty, Phys. Dark Universe **48**, 101958 (2025)
37. S. Capozziello, V.F. Cardone, A. Troisi, Phys. Rev. D **71**(4), 043503 (2005)
38. S. Nojiri, S.D. Odintsov, Int. J. Geom. Methods Mod. Phys. **4**(01), 115 (2007)
39. S. Nojiri, S.D. Odintsov, Phys. Lett. B **652**(5–6), 343 (2007)
40. G. Cognola, E. Elizalde, S. Nojiri, S.D. Odintsov, S. Zerbini, Phys. Rev. D **73**(8), 084007 (2006)
41. A. De Felice, S. Tsujikawa, Phys. Lett. B **675**(1), 1–8 (2009)
42. P. Wu, H. Yu, Phys. Lett. B **692**(3), 176 (2010)

43. Y. Zhang, H. Li, Y. Gong, Z.-H. Zhu, J. Cosmol. Astropart. Phys. **2011**(07), 015 (2011)
44. T. Harko, F.S. Lobo, G. Otalora, E.N. Saridakis, J. Cosmol. Astropart. Phys. **2014**(12), 021 (2014)
45. M. De Laurentis, M. Paolella, S. Capozziello, Phys. Rev. D **91**(8), 083531 (2015)
46. M. Sharif, A. Ikram, Eur. Phys. J. C **76**, 640 (2016)
47. T. Harko, F.S. Lobo, S. Nojiri, S.D. Odintsov, Phys. Rev. D **84**(2), 024020 (2011)
48. M. Houndjo, Int. J. Mod. Phys. D **21**(01), 1250003 (2012)
49. S. Chakraborty, Gen. Relativ. Gravit. **45**, 2039 (2013)
50. R. Zaregonbadi, M. Farhoudi, N. Riazi, Phys. Rev. D **94**(8), 084052 (2016)
51. M.Z. Bhatti, Z. Yousaf, M. Yousaf, Chin. J. Phys. **77**, 2617 (2022)
52. B. Almutairi, M.Z. Bhatti, M. Yousaf et al., Int. J. Theor. Phys. **63**, 215 (2024)
53. P.K. Sahoo, P. Sahoo, B.K. Bishi, Int. J. Geom. Methods Mod. Phys. **14**(06), 1750097 (2017)
54. G. Carvalho, S. dos Santos Jr, P. Moraes, M. Malheiro, Int. J. Mod. Phys. D **29**(10), 2050075 (2020)
55. J.M. Pretel, S.E. Jorás, R.R. Reis, J.D. Arbañil, J. Cosmol. Astropart. Phys. **2021**(08), 055 (2021)
56. T. Naseer, Phys. Dark Universe **46**, 101663 (2024)
57. A. Rehman, M. Yousaf, F. Javed, P. Channuie, Eur. Phys. J. C **85**, 949 (2025)
58. A. Ditta, G. Mustafa, A. Mahmood, J. High Energy Astrophys. **45**, 350 (2025)
59. U. Farwa, A. Abbas, M. Yousaf, Nucl. Phys. B **1018**, 117086 (2025)
60. A. Rehman, T. Naseer, N. Alessa, A.-H. Abdel-Aty, Nucl. Phys. B **1015**, 116897 (2025)
61. L. Flamm, Physikalische Zeitschrift **17**, 448 (1916)
62. A. Einstein, N. Rosen, Phys. Rev. **48**(1), 73 (1935)
63. H.G. Ellis, J. Math. Phys. **14**, 104 (1973)
64. K. Bronnikov, Scalar-tensor theory and scalar charge. Acta. Phys. Pol. B4 (1973)
65. M.S. Morris, K.S. Thorne, U. Yurtsever, Phys. Rev. Lett. **61**(13), 1446 (1988)
66. D. Hochberg, M. Visser, Null energy condition in dynamic wormholes. Phys. Rev. Lett. **81**(4), 746 (1998)
67. D. Hochberg, M. Visser, Phys. Rev. D **58**(4), 044021 (1998)
68. E. Teo, Phys. Rev. D **58**(2), 024014 (1998)
69. K. Nandi, B. Bhattacharjee, S. Alam, J. Evans, Phys. Rev. D **57**(2), 823 (1998)
70. A. Bhattacharya, I. Nigmatzyanov, R. Izmailov, K.K. Nandi, Class. Quantum Gravity **26**(23), 235017 (2009)
71. M. Yousaf, M.Z. Bhatti, Z. Yousaf, Nucl. Phys. B **995**, 116328 (2023)
72. M.Z. Bhatti, Z. Yousaf, M. Yousaf, Commun. Theor. Phys. **75**, 125401 (2023)
73. M. Yousaf, H. Asad, K.A. Yasir, S. Maurya, A. Ali, F. Atamurotov, Eur. Phys. J. C **85**(11), 1352 (2025)
74. K. Bronnikov, S.-W. Kim, Phys. Rev. D **67**(6), 064027 (2003)
75. J.P. Lemos, F.S. Lobo, S.Q. de Oliveira, Phys. Rev. D **68**(6), 064004 (2003)
76. F. Rahaman, S. Chakraborty, M. Kalam, Int. J. Mod. Phys. D **16**(10), 1669 (2007)
77. C.G. Böhmer, T. Harko, F.S. Lobo, Phys. Rev. D **76**(8), 084014 (2007)
78. E. Dai, M. Yousaf, F. Javed, M. Shrahili, R.M. Zulqarnain, Nucl. Phys. B **1018**, 117017 (2025)
79. O.A. Almatroud, M. Rizwan, M.Z. Bhatti, M. Alshammari, S. Alshammari, Z. Yousaf, Phys. Dark Universe **50**, 102135 (2025)
80. O.A. Almatroud, M. Rizwan, M. Alshammari, M.Z. Bhatti, S. Alshammari, Z. Yousaf, Eur. Phys. J. C **85**, 1285 (2025)
81. Z. Yousaf, M. Rizwan, M. Alshammari, O.A. Almatroud, S. Alshammari, M.M. Al-sawalha, Eur. Phys. J. C **85**, 1 (2025)
82. M.H. Daouda, M.E. Rodrigues, M. Houndjo, Eur. Phys. J. C **71**, 1817 (2011)
83. A. Ditta, S. Sadiq, A. Rasheed, A. Errehymy, S.K. Maurya, G. Mustafa, Int. J. Geom. Methods Mod. Phys. **0**, 2550182 (2025)
84. A. Saleem, Z. Ali, A. Bouzenada, A. Ditta, F. Atamurotov, G. Mustafa, Nucl. Phys. B **1018**, 117008 (2025)
85. T. Harko, F.S. Lobo, M. Mak, S.V. Sushkov, Phys. Rev. D **87**(6), 067504 (2013)
86. C. Bambi, A. Cardenas-Avendano, G.J. Olmo, D. Rubiera-Garcia, Phys. Rev. D **93**(6), 064016 (2016)
87. P. Moraes, P. Sahoo, Eur. Phys. J. C **79**, 677 (2019)
88. P. Sahoo, S. Mandal, P. Sahoo, New Astron. **80**, 101421 (2020)
89. C. Chawla, A. Dixit, A. Pradhan, Can. J. Phys. **99**(8), 634 (2021)
90. T. Tangphati, A. Banerjee, A. Pradhan, Int. J. Geom. Methods Mod. Phys. **21**, 2450109 (2024)
91. C.G. Boehmer, T. Harko, F.S. Lobo, Phys. Rev. D **85**(4), 044033 (2012)
92. M. Jamil, D. Momeni, R. Myrzakulov, Eur. Phys. J. C **73**, 2267 (2013)
93. A. Banerjee, M. Jasim, S.G. Ghosh, Ann. Phys. **433**, 168575 (2021)
94. A. Waseem, F. Javed, M.Z. Gul, G. Mustafa, A. Errehymy, Eur. Phys. J. C **83**, 1088 (2023)
95. M.Z. Bhatti, M. Yousaf, Z. Yousaf, New Astron. **106**, 102132 (2024)
96. T. Naseer, M. Sharif, M. Faiza, Int. J. Geom. Methods Mod. Phys. **22**, 2440043 (2025)
97. M. Yousaf, H. Asad, Phys. Dark Universe **48**, 101841 (2025)
98. M. Barriola, A. Vilenkin, Phys. Rev. Lett. **63**(4), 341 (1989)
99. M. Yousaf, I. Shahid, O. Rahimov, A. Alqahtani, Int. J. Geom. Methods Mod. Phys. 2650060 (2025). https://doi.org/10.1142/S021988782650060X
100. M. Yousaf, H. Asad, A. Rehman, M.R. Shahzad et al., Phys. Dark Universe **50**, 102123 (2025)
101. H. Asad, M. Yousaf, U. Zafar et al., Fort. der Physik **73**, e70034 (2025)
102. J. Goswami, H. Rahman, R. Sikdar, R. Parvin, F. Ahmed, Eur. Phys. J. C **84**, 1037 (2024)
103. D.J. Gogoi, U.D. Goswami, J. Cosmol. Astropart. Phys. **2023**, 027 (2023)
104. M. Yousaf, B.S. Alkahtani, G. Mustafa, S.K. Maurya, Chin. J. Phys. **97**, 1255 (2025)
105. M. Yousaf, Int. J. Geom. Methods Mod. Phys. 2650099 (2025). https://doi.org/10.1142/S0219887826500994
106. F. Ahmed, Sci. Rep. **13**(1), 12953 (2023)
107. F. Rahaman, S. Sarkar, K.N. Singh, N. Pant, Mod. Phys. Lett. A **34**(01), 1950010 (2019)